



Publication Year	2017
Acceptance in OA @INAF	2020-09-10T07:39:46Z
Title	The VIMOS Public Extragalactic Redshift Survey (VIPERS). Downsizing of the blue cloud and the influence of galaxy size on mass quenching over the last eight billion years
Authors	Haines, C. P.; IOVINO, Angela; Krywult, J.; Guzzo, L.; Davidzon, I.; et al.
DOI	10.1051/0004-6361/201630118
Handle	http://hdl.handle.net/20.500.12386/27265
Journal	ASTRONOMY & ASTROPHYSICS
Number	605

The VIMOS Public Extragalactic Redshift Survey (VIPERS)

Downsizing of the blue cloud and the influence of galaxy size on mass quenching over the last eight billion years[★]

C. P. Haines¹, A. Iovino¹, J. Krywult², L. Guzzo^{1,3}, I. Davidzon^{4,5}, M. Bolzonella⁵, B. Garilli⁶, M. Scodeggio⁶, B. R. Granett¹, S. de la Torre⁴, G. De Lucia⁷, U. Abbas⁸, C. Adami⁴, S. Arnouts^{4,19}, D. Bottini⁶, A. Cappi^{5,10}, O. Cucciati^{9,5}, P. Franzetti⁶, A. Fritz⁶, A. Gargiulo⁶, V. Le Brun⁴, O. Le Fèvre⁴, D. Maccagni⁶, K. Małek¹¹, F. Marulli^{9,12,5}, T. Moutard^{25,4}, M. Polletta^{6,13,14}, A. Pollo^{15,11}, L. A. M. Tasca⁴, R. Tojeiro¹⁶, D. Vergani^{17,5}, A. Zanicelli¹⁸, G. Zamorani⁵, J. Bel²⁰, E. Branchini^{21,22,23}, J. Coupon²⁴, O. Ilbert⁴, L. Moscardini^{9,12,5}, J. A. Peacock²⁶, and M. Siudek²⁷

(Affiliations can be found after the references)

Received 22 November 2016 / Accepted 28 March 2017

ABSTRACT

We use the full VIPERS redshift survey in combination with SDSS-DR7 to explore the relationships between star-formation history (using d4000), stellar mass and galaxy structure, and how these relationships have evolved since $z \sim 1$. We trace the extents and evolutions of both the blue cloud and red sequence by fitting double Gaussians to the d4000 distribution of galaxies in narrow stellar mass bins, for four redshift intervals over $0 < z < 1$. This reveals downsizing in star formation, since the high-mass limit of the blue cloud has retreated steadily with time from $M \sim 10^{11.2} M_{\odot}$ at $z \sim 0.9$ to $M \sim 10^{10.7} M_{\odot}$ by the present day. The number density of massive blue-cloud galaxies ($M > 10^{11} M_{\odot}$, $d4000 < 1.55$) drops sharply by a factor five between $z \sim 0.8$ and $z \sim 0.5$. These galaxies are becoming quiescent at a rate that largely matches the increase in the numbers of massive passive galaxies seen over this period. We examine the size-mass relation of blue-cloud galaxies, finding that its high-mass boundary runs along lines of constant M/r_e or equivalently inferred velocity dispersion. Larger galaxies can continue to form stars to higher stellar masses than smaller galaxies. As blue-cloud galaxies approach this high-mass limit, entering a narrow diagonal region within the size-mass plane termed the “quenching zone”, they start to be quenched, their d4000 values increasing to push them towards the green valley. In parallel, their structures change, showing higher Sérsic indices and central stellar mass densities. For these galaxies, bulge growth is required for them to reach the high-mass limit of the blue cloud and be quenched by internal mechanisms. The blue-cloud galaxies that are being quenched at $z \sim 0.8$ lie along the same size-mass relation as present day quiescent galaxies and seem the likely progenitors of today’s S0s.

Key words. galaxies: evolution – galaxies: star formation – galaxies: structure – galaxies: stellar content

1. Introduction

The recent wide-field surveys such as the Sloan Digital Sky Survey (SDSS) have firmly established that galaxies in the local Universe can be broadly divided into two distinct populations according to their ultraviolet-optical colours: the blue cloud made up of young, star-forming galaxies; and the red sequence of passively-evolving galaxies that becomes increasingly dominant with stellar mass (Strateva et al. 2001; Baldry et al. 2004; Wyder et al. 2007; Blanton & Moustakas 2009; Taylor et al. 2015). This bimodality in colour (or star-formation activity) and

its mass-dependence has been shown to persist to at least $z \sim 4$ (Pozzetti et al. 2010; Muzzin et al. 2013; Ilbert et al. 2013; Tomczak et al. 2014), with star-forming galaxies following a tight relation between star formation rate (SFR) and stellar mass (M ; Noeske et al. 2007; Speagle et al. 2014; Lee et al. 2015).

This dichotomy in colour is deeply entwined with the well-known structural bimodality of galaxies, which can broadly be separated into smooth early-types and disc-dominated spirals (Hubble 1926; Sandage 1961; Kormendy & Bender 2012). The bivariate distribution of galaxies in the colour-Sérsic index (η) plane reveals two distinct peaks that correspond with blue, star-forming discs and red, quiescent bulges (Driver et al. 2006; Ball et al. 2007), up to $z \sim 2$ (Bruce et al. 2014; Krywult et al. 2017). The star-formation activity of galaxies in the local Universe has been found to correlate more strongly with mean stellar mass density (Σ_e ; Kauffmann et al. 2003a, 2006; Brinchmann et al. 2004), the presence of a bulge (Bell 2008), and the stellar mass density within the central kpc (Σ_1 ; Fang et al. 2013) than with stellar mass. Omand et al. (2014) find that the fraction of quiescent galaxies correlates best with $M/r_e^{3/2}$. These correlations have been found to persist up to $z \sim 3$ (Franx et al. 2008; Wuyts et al. 2011; Cheung et al. 2012; Bell et al. 2012; Lang et al. 2014; Barro et al. 2017; Whitaker et al. 2017). These correlations

[★] Based on observations collected at the European Southern Observatory, Cerro Paranal, Chile, using the Very Large Telescope under programs 182.A-0886 and partly 070.A-9007. Also based on observations obtained with MegaPrime/MegaCam, a joint project of CFHT and CEA/DAPNIA, at the Canada-France-Hawaii Telescope (CFHT), which is operated by the National Research Council (NRC) of Canada, the Institut National des Sciences de l’Univers of the Centre National de la Recherche Scientifique (CNRS) of France, and the University of Hawaii. This work is based in part on data products produced at TERAPIX and the Canadian Astronomy Data Centre as part of the Canada-France-Hawaii Telescope Legacy Survey, a collaborative project of NRC and CNRS. The VIPERS web site is <http://www.vipers.inaf.it/>

suggest that the internal structure of a galaxy, and its development, must play a crucial role in driving or regulating its star-formation activity, although Lilly & Carollo (2016) show how these correlations can arise naturally, even in cases where structure plays no physical role.

The total stellar mass content of galaxies has approximately doubled since $z \sim 1.0$ – 1.2 (e.g. Muzzin et al. 2013; Ilbert et al. 2013; Tomczak et al. 2014). This growth in the integrated stellar mass contained within galaxies has been found to be in good agreement with the cosmic SFR integrated over the same period (Bell et al. 2007; Ilbert et al. 2013). However, while these new stars are being formed within the blue cloud, the build-up of stellar mass is largely confined to the red sequence population of quiescent galaxies (Arnouts et al. 2007; Tomczak et al. 2014), while the integrated stellar mass within the star-forming galaxy population has remained approximately constant since $z \sim 1$ (Bell et al. 2007; Ilbert et al. 2010; Pozzetti et al. 2010).

If the massive blue-cloud galaxies observed at $z \sim 1$ were to continue growing by forming stars at rates given by the evolving SFR– M relation of normal star-forming galaxies through to the present day, this would leave a large population of massive $\gtrsim 10^{11} M_{\odot}$ spiral galaxies at $z \sim 0$ (Bell et al. 2007). This population is simply not seen in the local Universe. Instead, the maximum stellar mass of actively star-forming galaxies was observed by Cowie et al. (1996) to have fallen steadily from $z \sim 1$ to lower redshifts, a process they call “downsizing”. This term has since been used to describe a variety of seemingly anti-hierarchical behaviours within galaxy populations (Fontanot et al. 2009), such as the finding that massive quiescent galaxies have stellar populations that formed earlier and over shorter time-scales than lower-mass systems (e.g. Thomas et al. 2005). This can lead to confusion. Here we refer to downsizing in the original sense of Cowie et al. (1996).

Something is required to shut down star formation in massive blue cloud galaxies at a high enough rate to ensure that the stellar mass function (SMF) of star-forming galaxies remains approximately unchanged since $z \sim 1$ (Pozzetti et al. 2010; Moutard et al. 2016b), and to enable the high-mass end of the red sequence to build up rapidly over the same period (Davidzon et al. 2013; Fritz et al. 2014). Peng et al. (2010) show that to keep the blue cloud SMF unchanged requires a mechanism that terminates star formation in massive galaxies at a rate that is statistically proportional to their SFR. This process is loosely termed “mass quenching” and is believed to be the dominant mechanism for terminating star formation among high-mass ($\gtrsim 10^{10.5} M_{\odot}$) blue cloud galaxies, while environment-related processes become more important at lower stellar masses (e.g. Haines et al. 2007; Mahajan et al. 2010). In this work, we focus on those quenching processes that act internally on the galaxy (including its circumgalactic medium) and which define the limiting galaxy properties beyond which they cannot continue growing through forming stars. We do not consider environmental effects further.

A variety of physical mechanisms have been proposed that could be responsible for quenching star formation in blue-cloud galaxies once they reach a certain mass (Gabor et al. 2010). Feedback from an active galactic nucleus (AGN) has been frequently invoked to limit the growth of massive galaxies and produce the turnover in the SMF by suppressing gas cooling (Bower et al. 2006). Gas-rich galaxy mergers channel large amounts of gas onto the central nucleus, fuelling powerful starbursts and rapid black hole growth, until feedback from accretion is able to drive quasar winds and expel the remaining gas from the galaxy, quenching star formation (Di Matteo et al. 2005; Hopkins et al. 2006). Subsequent low-level “radio mode” AGN feedback may

then prevent the hot gas corona from cooling and reinitiating star formation (Croton et al. 2006).

Martig et al. (2009) propose that the build up of a central mass concentration or bulge within a massive star-forming galaxy could stabilize the gas disc against fragmentation and collapse into molecular gas clouds, and morphologically quench its star formation from the inside-out (Genzel et al. 2014). Low-level feedback from the winds of asymptotic giant branch (AGB) stars could contribute to prevent the residual gas from cooling in dense, early-type galaxies, keeping them quiescent (Conroy et al. 2015). The evolution of a galaxy is also thought to depend on the mass of the dark matter (DM) halo that hosts it, through the transition from low-mass halos, where narrow streams of cold gas continually feed the galaxy with new fuel for star formation, to DM haloes more massive than $\sim 10^{12} M_{\odot}$, where stable virial shocks form, heating the infalling gas to the virial temperature ($\sim 10^6$ K) and dramatically reducing the accretion rate of gas onto the galaxy (Kereš et al. 2005; Dekel & Birnboim 2006; Dekel et al. 2009).

The star formation history of a galaxy is fundamentally written within its spectrum, comprising both emission lines from gas ionized by the ultraviolet photons of short-lived hot O and B stars, representing the current SFR, and the stellar continuum produced by evolved stars. This continuum contains a complex array of spectral features and absorption lines that encode many details of the stellar demographics. One of the most direct methods for characterising the star formation history of galaxies is measuring the 4000 Å spectral break (hereafter d4000), the strongest discontinuity in the optical spectrum of a galaxy. The strong break occurs in older stellar populations owing to a sudden accumulation of absorption features blueward of 4000 Å (e.g. CaII H+K lines) that appear in stars cooler than G0 (6000 K) as a result of ionized metals (Gorgas et al. 1999). In hotter stars, elements are multiply ionized and the opacity decreases, so the break appears much smaller ($d4000 \approx 1.0$ – 1.4). Since hot stars are short-lived, the d4000 index increases monotonically with stellar age. Kauffmann et al. (2003b) show that it is an excellent age indicator, in particular for young (< 1 Gyr, $d4000 < 1.5$) stellar populations, where it does not depend strongly on metallicity. For stronger 4000 Å breaks characteristic of quiescent galaxies with old stellar populations ($d4000 > 1.6$), the d4000 index depends significantly on metallicity as well as age (Kauffmann et al. 2003b; Siudek et al. 2017).

Brinchmann et al. (2004) show that d4000 may also be used as a proxy for specific-SFR (SFR/M). Kauffmann et al. (2003a) show that galaxies in the local Universe can be split into two well-separated populations: low-mass galaxies with young stellar populations ($d4000 < 1.55$), low surface mass densities, and Sérsic indices typical of discs; and high-mass galaxies with old stellar populations ($d4000 > 1.55$), high stellar mass densities, and concentrations. Later studies that combined d4000 with a range of age and metallicity-dependent spectral indices to obtain more robust constraints on the light-weighted stellar ages of galaxies, confirmed that the bimodality in d4000 seen by Kauffmann et al. (2003a) indeed signifies a bimodality in stellar age (Gallazzi et al. 2005; Haines et al. 2006).

The key limitation of Kauffmann et al. (2003a) and other SDSS-based studies is that all the galaxies are at essentially the same redshift, so that we cannot follow the evolution of the observed trends between d4000 and M or galaxy structure over a cosmically significant time-scale, or determine when these trends were established. The present paper attempts to do this, taking advantage of the recently completed VIMOS Public Extragalactic Redshift Survey (VIPERS) to trace the bimodal

distribution of galaxies in the $d4000$ – M plane back to $z \sim 1$, and explore how the relationships between star-formation history, stellar mass, and galaxy structure have evolved over the last eight billion years.

The fundamental objective of the VIPERS project has been to provide a representative vision of the large-scale structure and the global properties of galaxies when the Universe was about half its current age (Guzzo et al. 2014), just as the SDSS survey has done for the local Universe. The availability of robust spectral parameters, including $d4000$ and $[OII]$, as well as stellar masses and structural parameters obtained from high-quality imaging from the Canada-France-Hawaii Telescope Legacy Survey Wide (CFHTLS-Wide¹), for a well-defined sample of almost 100 000 galaxies at $0.5 < z < 1.2$, allows the distributions of the global properties of galaxies to be mapped in fine detail. VIPERS uniquely provides large volume coverage at $0.5 < z < 1.2$, allowing the assembly of statistically representative samples of relatively rare massive galaxies above $10^{11} M_{\odot}$, and, in particular, those at the high-mass end of the blue cloud. The VIPERS survey and the local SDSS sample are described in Sect. 2.

Section 3 examines the evolution of the bimodal distribution of galaxies in the $d4000$ – M plane, and downsizing in the high-mass limit of the blue cloud. The evolution in the number density of massive blue-cloud galaxies is presented in Sect. 4. Section 5 presents the size-mass relations of blue-cloud galaxies, examining the dependencies of both $d4000$ and Sérsic index η on the effective radius and stellar mass of galaxies, and demonstrating how mass quenching is influenced also by galaxy size. The discussion and summary follow in Sects. 6 and 7. A concordance Λ CDM cosmology with $\Omega_M = 0.3$, $\Omega_{\Lambda} = 0.7$ and $H_0 = 70 \text{ km s}^{-1} \text{ Mpc}^{-1}$ is assumed throughout.

2. Data

VIPERS is a spectroscopic survey that was completed in 2015 and that has targeted $\sim 100\,000$ galaxies at $0.5 \lesssim z \lesssim 1.2$ over 23.5 deg^2 , split into two fields within the CFHTLS-Wide, namely W1 and W4. All details of the survey design, construction and scientific goals can be found in Guzzo et al. (2014). Spectroscopic targets were selected to have $17.5 \leq i_{AB} \leq 22.5$ (after correction for Galactic extinction), with a second selection criterion, based on $(u - g)$ and $(r - i)$ colours applied to exclude low-redshift ($z < 0.5$) objects.

All the spectroscopic observations for VIPERS were carried out using the Visible Multi-Object Spectrograph (VIMOS; Le Fèvre et al. 2003) on the 8.2 m Very Large Telescope (VLT) Unit 3, with the LR-Red grism which provides a spectral resolution $R \sim 220$ over the wavelength range 5500 – 9500 \AA at a dispersion of 7.3 \AA/pixel . To maximize the multiplex capability of VIMOS, the short-slit strategy of Scodreggio et al. (2009) was used. This enabled a target sampling rate of 47% to be reached with a single pass (Scodreggio et al. 2017). The reduction and redshift measurement is performed within a fully automated pipeline (Garilli et al. 2010, 2012, 2014), before each redshift is independently validated by two team members and its reliability quantified using the flag z_{flag} , following a scheme similar to that used for the VIMOS VLT Deep Survey (VVDS; Le Fèvre et al. 2005) and zCOSMOS (Lilly et al. 2007). From repeated measurements, typical redshift uncertainties of $\sigma_z = 0.00054(1 + z)$ are obtained (Scodreggio et al. 2017).

The dataset used in this paper is based on an internal pre-release of the final, complete VIPERS spectroscopic catalogue, the Second Public Data Release (PDR-2; Scodreggio et al. 2017). From this sample, we consider only the 75 479 galaxies with highly accurate redshift measurements, i.e. with $2 \leq z_{\text{flag}} \leq 9$ and $z > 0$. This excludes broad-line AGN, stars, and secondary objects that happened, by chance, to appear in the slit of a primary target. The strength of the 4000 \AA break was measured for all galaxies with reliable redshifts in the range $0.414 < z < 1.346$, which meant that the spectral feature was fully contained within the wavelength range covered by the VIMOS spectra (Garilli et al. 2014). We adopt the narrow definition of the amplitude of the 4000 \AA break introduced by Balogh et al. (1999), which is relatively insensitive to the effects of dust reddening. This is defined as the ratio of the average continuum flux density F_{ν} in the wavebands 4000 – 4100 \AA and 3850 – 3950 \AA . At $z < 0.5$ the VIPERS sample becomes highly incomplete owing to the $ugri$ colour cuts imposed in the selection of spectroscopic targets (Guzzo et al. 2014), while at $z > 1.1$, the survey becomes incomplete even at the highest stellar masses ($M > 10^{11} M_{\odot}$; Davidzon et al. 2013). We thus limit our analysis to redshifts $0.5 \leq z < 1.1$, giving a final sample of 65 142 galaxies with reliable redshifts and $d4000$ measurements, 43 607 in the W1 field and 21 535 in W4. The PDR-2 sample includes 450 additional reliable redshifts in the range $0.5 \leq z < 1.1$ that were validated after the analysis was completed, i.e. a difference of $< 1\%$ from the sample used in this paper.

Since it was only possible to obtain redshifts for $\sim 40\%$ of all possible targets, statistical weights are required to make this subsample representative of all $0.5 \leq z < 1.1$ galaxies within the parent photometric catalogue ($i_{AB} \leq 22.5$). For every galaxy in the final sample, the likelihood that it was targeted and a reliable redshift obtained is encoded through the target sampling rate (TSR) and spectroscopic success rate (SSR) parameters (for full details see Guzzo et al. 2014). The TSR is the fraction of galaxies within a given VIMOS quadrant that satisfy the selection criteria that were successfully placed behind a slit and observed, reflecting the localized variation in the spatial density of targets across the survey area. The SSR represents the probability of being able to obtain a reliable redshift for a galaxy that has been targeted, given its i_{AB} magnitude, redshift, and VIMOS quadrant.

For each galaxy in the VIPERS spectroscopic sample, improved photometric measurements have been obtained in the $ugriz$ bands from the T0007 release of the CFHTLS images and photometric catalogues of the W1 and W4 fields, combined with K_s photometry from the VIPERS Multi-Lambda Survey (VIPERS-MLS²; Moutard et al. 2016a), based on follow-up CFHT/WIRCam K_s -band imaging or from the VISTA Deep Extragalactic Observations (VIDEO; Jarvis et al. 2013) survey. Total stellar masses (M) and rest-frame colours are obtained using the updated *Hyperzmass* (Bolzonella et al. 2000, 2010) code, with a set-up similar to that used in Davidzon et al. (2016). The $ugrizK_s$ photometry of each galaxy is compared to a set of synthetic spectral energy distributions (SEDs) shifted by $1 + z_{\text{spec}}$. The SED library is built using the stellar population synthesis model of Bruzual & Charlot (2003), with a wide variety of star formation histories and adopting the universal initial mass function (IMF) of Chabrier (2003). Each template has a fixed metallicity ($Z = 0.004$ or $Z = 0.02$) and dust reddening that follows Calzetti et al. (2000) or Prévot-Bouchet (Prevot et al. 1984; Bouchet et al. 1985) attenuation curves (A_V ranging from 0 to 3).

¹ <http://www.cfht.hawaii.edu/Science/CFHTLS/>

² <http://cesam.lam.fr/vipers-mls/>

The code selects as best-fit SED the model that minimizes the χ^2 value. The stellar mass estimate is taken directly from the best-fit template. Absolute magnitudes in the rest-frame waveband λ_0 are computed starting from the apparent magnitude observed in the filter closest to $\lambda_0/(1+z)$, and then k -corrected using the model SED. This best-fit template is then artificially redshifted until the model galaxy has an apparent magnitude $i_{AB} = 22.5$, thus establishing the maximum redshift z_{\max} at which the galaxy could have been included in VIPERS. We derive the stellar mass completeness limits of the VIPERS survey as a function of both redshift and d4000 value, as described in Appendix A.

2.1. Structural parameters

Krywult et al. (2017) determined robust structural parameter measurements (e.g. r_e , η) for VIPERS galaxies with reliable redshifts ($2 \leq z_{\text{flag}} \leq 9$), fitting 2D PSF-convolved Sérsic profiles to the observed i -band light distribution of galaxies from the high-quality CFHTLS-Wide images (T0006 release). These $1^\circ \times 1^\circ$ images obtained with the MegaCam instrument have a $0.186''$ pixel scale and typical seeing of $0.64''$ FWHM. To accurately model the variation in the point spread function (PSF) across each $1^\circ \times 1^\circ$ MegaCam image, elliptical Moffat fits were performed for ~ 2000 isolated, bright, non-saturated stars that are distributed across the full image. Each fitted parameter of the Moffat function was then approximated by a 2D Chebyshev polynomial, enabling the local PSF to be generated at the position of each galaxy.

In this work we use the circularized i -band half-light radius (r_e) as a measure of each galaxy's size and the best-fit Sérsic index η as a measure of its structure. Krywult et al. (2017) fully tested the reliability of their structural parameter measurements by placing model galaxies within the CFHTLS images, from which they estimate uncertainties in their half-light radii of 4.4% (12%) for 68% (95%) of galaxies. Assuming that the stellar mass is distributed radially following the observed i -band light (i.e. there are no radial variations in the mass-to-light ratio within the galaxy), the effective stellar mass surface density is then defined as $\Sigma_e = M/(2\pi r_e^2)$. The central stellar mass surface density Σ_1 is estimated by integrating the best-fit Sérsic profile in two dimensions out to a radius of 1 kpc.

Approximately 13% of the VIPERS survey area was not covered by the structural parameter analysis of Krywult et al. (2017), while other galaxies are excluded owing to them having poor local PSFs, GALFIT not converging, or because the best-fit profile had $\eta < 0.2$, which is not physical. This results in a sample of 49 533 galaxies with reliable structural parameters (and reliable redshifts) or 76% of our full sample of 65 142. The likelihood that we were able to determine structural parameters for a galaxy shows no sign of depending on its properties (e.g. stellar mass) or redshift. The stellar mass and redshift distributions of those galaxies with reliable structural parameters are indistinguishable from the full sample.

2.2. SDSS comparison sample of local galaxies

For a comparison sample of local ($z \lesssim 0.1$) galaxies with available stellar masses, d4000 measurements, and structural parameters, we take the catalogue of Omand et al. (2014), which is based upon the 7th data release of the SDSS (SDSS-DR7; Abazajian et al. 2009), and matches the structural parameter measurements of Simard et al. (2011) with the stellar mass estimates and spectral index measurements (e.g. d4000)

from the MPA-JHA DR7 catalogues (Kauffmann et al. 2003b; Brinchmann et al. 2004; Salim et al. 2007). We consider only those galaxies within the contiguous region of the North Galactic Cap, which covers $\sim 7500 \text{ deg}^2$. These stellar masses assume a Kroupa IMF, and so we reduce them by 10% to correct their mass-to-light ratios to the Chabrier (2003) IMF used here.

For direct comparison to our structural parameters, we take the r -band half-light circularized effective radii (r_e) and Sérsic index η from the best-fit PSF-convolved pure Sérsic profiles obtained by Simard et al. (2011) using GIM2D. Simard et al. (2011) also performed full bulge-disc decompositions, with $\eta = 4$ bulge and exponential disc components, from which we take their measurements of the fraction of r -band light in the bulge component (B/T). The faint galaxy magnitude limit of the SDSS spectroscopic survey is $r_{\text{Petro}} = 17.77$, while Simard et al. (2011) apply a bright galaxy cut at $r_{\text{Petro}} = 14.0$. This results in incompleteness, both at low masses ($\lesssim 10^{10} M_\odot$) for $z \gtrsim 0.055$, but also at the very highest stellar masses ($\gtrsim 10^{11} M_\odot$) within $z \sim 0.04$.

3. The bimodal d4000 distribution of galaxies and its evolution from $z = 1.0$ to the present day

Figure 1 shows the d4000 distributions of galaxies, sliced into 0.2 dex wide bins of stellar mass, in four redshift ranges from $z = 1$ to the present day, combining VIPERS and SDSS datasets. The VIPERS survey is split into three redshift ranges: 0.8–1.0, 0.65–0.80, and 0.50–0.65 (panels a–c) that span approximately equal periods of time (0.89, 0.81, and 0.97 Gyr respectively). To allow a direct comparison with galaxies in the local Universe, Fig. 1d presents the d4000 distributions of $0.02 \leq z < 0.08$ galaxies from SDSS-DR7 divided into the same stellar mass bins. The mean redshifts of these four bins are $\langle z \rangle = 0.90, 0.73, 0.58$, and 0.06 respectively.

The d4000 distributions, $f(x)$, for each stellar mass bin (coloured curves) are estimated using the adaptive kernel estimator (Silverman 1986), with each galaxy represented by a Gaussian kernel whose width σ_i is proportional to $f(x_i)^{-1/2}$, where x_i is the d4000 value of that galaxy. By matching the level of smoothing to the density of information, the adaptive kernel gives an objective and non-parametric estimator of the underlying distribution of a set of points, optimised to identify sub-structure and bimodality (Pisani 1993). We show also histograms of the d4000 distributions to give confidence that the adaptive kernel estimator is reliably mapping the data.

For the first three redshift intervals, every VIPERS galaxy is weighted by the TSR and SSR to reflect the probability it was targeted and a reliable redshift obtained. At lower stellar masses, galaxies are missed owing to being too faint to have been targeted by VIPERS ($i_{AB} > 22.5$). We statistically account for these missing galaxies by weighting each VIPERS galaxy according to the fraction of the total volume within that redshift interval for which it would still be included in VIPERS (based on its z_{\max} value), following the $1/V_{\max}$ method (Schmidt 1968). To account for stellar mass incompleteness in the SDSS sample, each galaxy in Fig. 1d is weighted according to the fraction of the total volume within $0.02 \leq z < 0.08$, where it would have $14.0 \leq r_{\text{Petro}} < 17.77$. The area under each curve is normalized to unity, so the curves describe the probability distribution of d4000 within that stellar mass bin. The curves become dotted when $< 90\%$ of the galaxies at a given d4000, stellar mass bin, and redshift interval are expected to be brighter than the $i_{AB} = 22.5$ mag survey limit. In other words, the solid curves indicate regions of parameter space above the 90% stellar mass completeness limits of the VIPERS survey (dashed curves in Fig. 2).

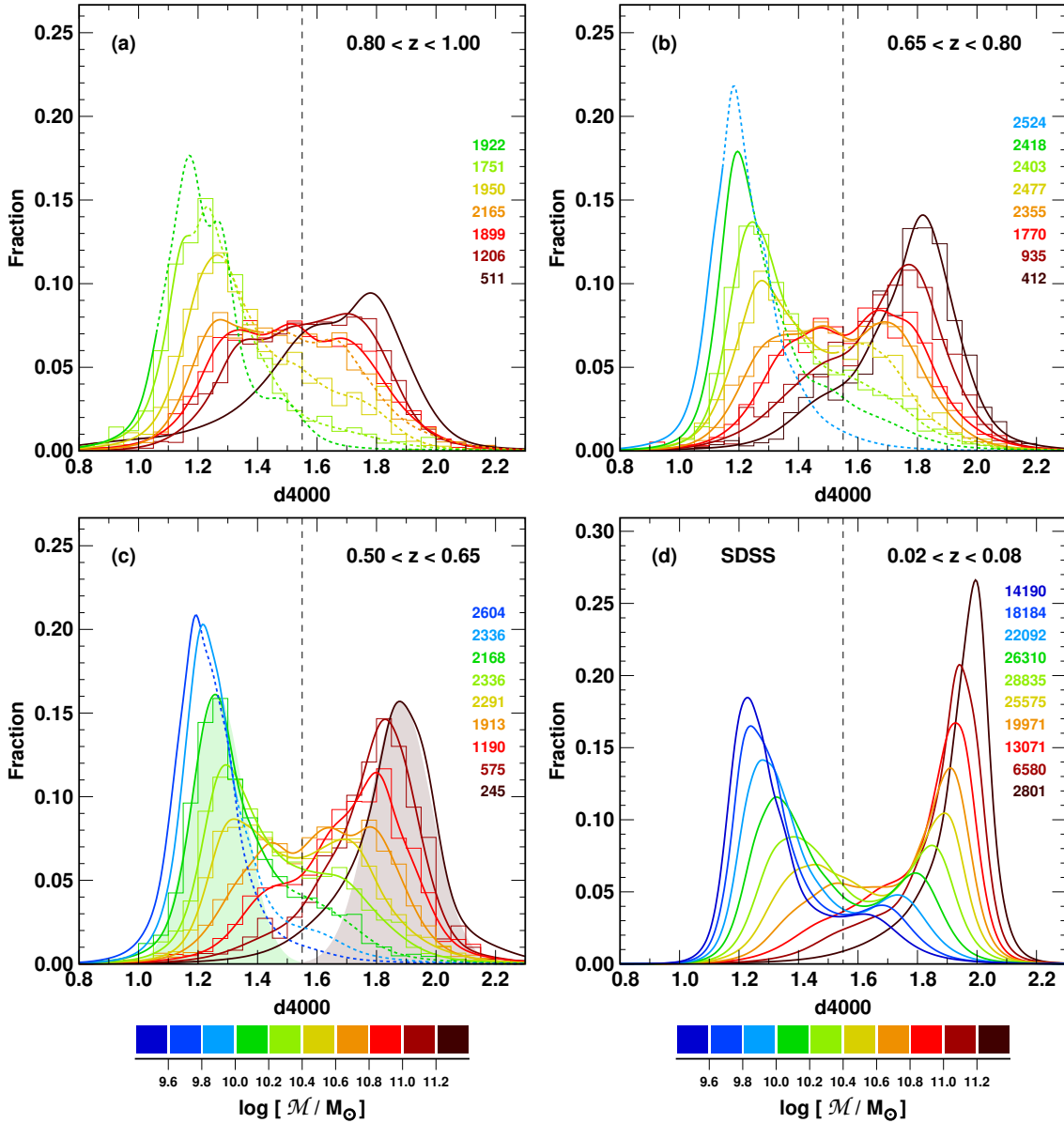


Fig. 1. Bimodal d4000 distribution of galaxies as a function of stellar mass and redshift. *Panels a–c* show the d4000 distribution of VIPERS galaxies in 0.2 dex wide bins of stellar mass (coloured curves), colour coded as indicated for three redshift bins: 0.8–1.0, 0.65–0.80, and 0.50–0.65. *Panel d* does the same, but for galaxies at $0.02 \leq z < 0.08$ taken from SDSS-DR7. The curves become dotted in regions of parameter space below the 90% stellar mass completeness limits of the VIPERS survey, shown as the dashed curves in Fig. 2. For some stellar mass bins, the d4000 distributions are also shown via histograms with bins of width 0.05 in d4000. The y-axis scale indicates the fraction of galaxies within these bins of width 0.05 in d4000. The coloured numbers down the *right-hand side* indicate the number of galaxies in each stellar mass bin. The vertical dashed line indicates the $d4000 = 1.55$ limit used to separate the blue cloud and red sequence galaxy populations. Example Gaussian fits to the d4000 distributions of blue cloud and red sequence populations in a single mass bin are shown by the solid coloured areas.

Figure 1 shows the development of bimodality in the d4000 distribution over the last eight billion years. At $0.8 \leq z < 1.0$ (Fig. 1a) there is a robust peak at $d4000 \approx 1.2$ that indicates the blue cloud, but only a weak possible peak at $d4000 \approx 1.8$ to indicate the red sequence in the highest stellar mass bin. Otherwise the red sequence appears more as a flat shelf in the subsequent stellar mass bins (orange/red curves). Less than 1 Gyr later at $0.65 \leq z < 0.8$ (Fig. 1b), the bimodality is now established with a clear peak at $d4000 \approx 1.8$ in the highest two stellar mass bins ($\log_{10} M \geq 11.0$). The height of the peak for the red sequence continues to rise with time through Figs 1c and d, as does the number of stellar mass bins where this peak is seen. The bimodality gets continually stronger with time, while the

valley between the two peaks gets steadily deeper and wider up to the present day. This bimodality allows us to robustly separate galaxies into blue cloud and red sequence populations in the VIPERS data by splitting the sample at a d4000 value of 1.55 (dashed line), midway between the two peaks at $0.50 \leq z < 0.65$ (Fig. 1c). This appears a reasonable choice also at higher redshifts (Figs. 1a,b), and is the same limit used by Kauffmann et al. (2003a) to separate young and old galaxies in the SDSS survey. At all redshifts, the relative fraction of galaxies in the blue cloud decreases with increasing stellar mass, while that in the red sequence increases. Both blue cloud and red sequence populations systematically shift to larger d4000 values with increasing stellar mass.

Table 1. Central d4000 values and 1σ widths of the best-fit Gaussian functions to the blue cloud and red sequence populations as a function of stellar mass for the three VIPERS redshift intervals.

log (M/M_{\odot})	Blue cloud population						Red sequence population					
	$0.50 \leq z < 0.65$		$0.65 \leq z < 0.80$		$0.80 \leq z < 1.00$		$0.50 \leq z < 0.65$		$0.65 \leq z < 0.80$		$0.80 \leq z < 1.00$	
	$\langle d4000 \rangle$	σ_{d4000}	$\langle d4000 \rangle$	σ_{d4000}	$\langle d4000 \rangle$	σ_{d4000}	$\langle d4000 \rangle$	σ_{d4000}	$\langle d4000 \rangle$	σ_{d4000}	$\langle d4000 \rangle$	σ_{d4000}
09.10	1.152	0.094	1.084	0.100	–	–	–	–	–	–	–	–
09.20	1.162	0.089	1.110	0.095	–	–	–	–	–	–	–	–
09.30	1.186	0.094	1.107	0.081	–	–	–	–	–	–	–	–
09.40	1.196	0.091	1.148	0.092	1.109	0.102	–	–	–	–	–	–
09.50	1.206	0.085	1.164	0.090	1.126	0.121	–	–	–	–	–	–
09.60	1.210	0.081	1.176	0.088	1.131	0.093	–	–	–	–	–	–
09.70	1.216	0.093	1.173	0.072	1.154	0.092	–	–	–	–	–	–
09.80	1.220	0.095	1.192	0.088	1.167	0.094	–	–	–	–	–	–
09.90	1.227	0.085	1.203	0.089	1.172	0.081	–	–	–	–	–	–
10.00	1.240	0.085	1.200	0.087	1.188	0.089	–	–	–	–	–	–
10.10	1.264	0.091	1.216	0.084	1.200	0.111	–	–	–	–	–	–
10.20	1.287	0.098	1.226	0.090	1.212	0.116	1.570	0.149	–	–	–	–
10.30	1.306	0.097	1.262	0.112	1.234	0.119	1.625	0.153	–	–	–	–
10.40	1.310	0.095	1.277	0.116	1.256	0.121	1.680	0.115	–	–	–	–
10.50	1.320	0.093	1.288	0.110	1.266	0.121	1.690	0.144	1.620	0.136	–	–
10.60	1.425	0.154	1.290	0.101	1.270	0.117	1.694	0.150	1.650	0.144	1.635	0.132
10.70	1.450	0.140	1.376	0.144	1.276	0.133	1.762	0.126	1.665	0.157	1.645	0.119
10.80	1.460	0.144	1.404	0.149	1.310	0.115	1.780	0.127	1.686	0.168	1.645	0.140
10.90	1.470	0.119	1.428	0.146	1.355	0.127	1.781	0.120	1.686	0.165	1.675	0.144
11.00	–	–	1.470	0.153	1.380	0.132	1.793	0.134	1.750	0.135	1.700	0.123
11.10	–	–	–	–	1.400	0.138	1.831	0.121	1.763	0.124	1.695	0.144
11.20	–	–	–	–	1.470	0.161	1.862	0.111	1.772	0.141	1.750	0.148
11.30	–	–	–	–	–	–	1.885	0.108	1.812	0.119	1.790	0.119
11.40	–	–	–	–	–	–	–	–	1.832	0.093	1.775	0.144

At low-to-intermediate stellar masses ($M \leq 10^{10.6} M_{\odot}$), the d4000 distribution of blue cloud galaxies can be well described by a Gaussian function in all four redshift bins. Where the red sequence shows a strong peak, it also has a Gaussian-like form. Following Baldry et al. (2004), we fit double Gaussians to the d4000 distributions of each stellar mass bin, allowing us to derive the central d4000 values and dispersions for both blue cloud and red sequence populations (Tables 1 and 2).

At higher stellar masses ($10.6 \lesssim \log_{10} M \lesssim 11.0$), the blue cloud becomes comparable in strength or sub-dominant to the red sequence, appearing as either a small hump or a flat shelf in the d4000 distribution at $d4000 \simeq 1.4$ – 1.5 . This feature is sufficiently prominent to allow the central d4000 value of the blue cloud to be fitted, and the low-d4000 side modelled by a Gaussian function, enabling its standard deviation to be estimated. At these stellar masses there is no obvious green valley: the d4000 distribution remains flat or rising through to the red sequence, suggestive of a continuous flow of quenching galaxies leaving the blue cloud and moving across to build up the red sequence. The typical uncertainties in the d4000 values of galaxies at these stellar mass ranges are ~ 0.05 (0.07) for those in the blue cloud in the $0.50 \leq z < 0.65$ ($0.80 \leq z < 1.0$) redshift bin, rising slightly to ~ 0.08 (0.10) in the red sequence, and hence are not sufficiently high to smooth away any green valley.

In the very highest stellar mass bin(s) ($\log_{10} M > 11.0$), the blue cloud appears no more than an extended low-d4000 tail of the dominant red sequence, and there is no feature enabling the central d4000 value of the blue cloud to be constrained. The blue-cloud galaxies appear too rare to allow us to define the d4000 distribution of the blue cloud population in any meaningful way. The upper limit of the blue cloud in each redshift slice

Table 2. Central d4000 values and 1σ widths of the best-fit Gaussian functions to the blue cloud and red sequence populations as a function of stellar mass for $0.02 \leq z < 0.08$ SDSS galaxies.

log (M/M_{\odot})	Blue-cloud galaxies		Red sequence galaxies	
	$\langle d4000 \rangle$	σ_{d4000}	$\langle d4000 \rangle$	σ_{d4000}
09.05	1.204	0.076	–	–
09.15	1.207	0.071	–	–
09.25	1.216	0.079	–	–
09.35	1.226	0.072	–	–
09.45	1.231	0.074	–	–
09.55	1.243	0.085	1.610	0.132
09.65	1.252	0.087	1.650	0.119
09.75	1.261	0.083	1.680	0.102
09.85	1.281	0.091	1.710	0.106
09.95	1.304	0.100	1.745	0.098
10.05	1.330	0.110	1.780	0.098
10.15	1.351	0.123	1.805	0.081
10.25	1.387	0.138	1.827	0.089
10.35	1.418	0.137	1.852	0.089
10.45	1.454	0.155	1.867	0.090
10.55	1.465	0.140	1.882	0.081
10.65	1.510	0.153	1.891	0.087
10.75	–	–	1.901	0.083
10.85	–	–	1.913	0.081
10.95	–	–	1.926	0.074
11.05	–	–	1.937	0.072
11.15	–	–	1.951	0.070
11.25	–	–	1.974	0.062
11.35	–	–	1.981	0.053
11.52	–	–	2.011	0.049

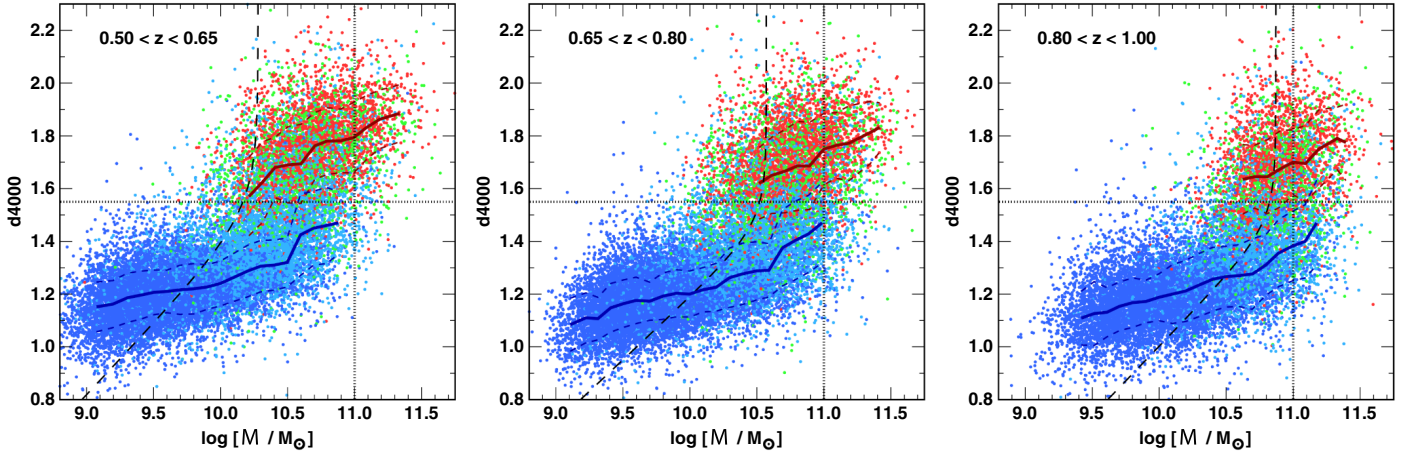


Fig. 2. d4000 versus stellar mass relation of VIPERS galaxies in three redshift bins: 0.50–0.65, 0.65–0.80, and 0.80–1.00. Galaxies are colour coded according to their location in the NUVrK diagram of Moutard et al. (2016b): red points indicate passive galaxies, green points mark those in the green valley, and blue points for those classified as star-forming. Dark blue points mark galaxies with [OII] emission detected at $>3\sigma$. Solid red and blue curves show the central d4000 values of the red sequence and blue cloud populations as a function of stellar mass, while the dashed curves mark the 1σ widths of each sequence. Black dashed curves mark the 90% stellar mass completeness limit as a function of d4000 for galaxies within that redshift interval. Horizontal and vertical dotted lines indicate the $d4000 = 1.55$ divider and $\log M = 11.0$ mass limit.

is determined as the highest stellar mass bin, where a Gaussian function can be fitted to the d4000 distribution at $d4000 < 1.55$.

Figure 2 shows the distribution of galaxies in the d4000– M plane for the same three redshift ranges. Solid curves show the central d4000 values of the blue and red sequences obtained from the double Gaussian fits as a function of mass, while the dashed lines indicate the 1σ widths of each sequence. Galaxies are colour coded according to their location in the NUVrK (NUV– r versus $r-K$) colour–colour diagram, applying the same delimiting cuts as Moutard et al. (2016b) to split the NUVrK diagram into three regions, which enables galaxies to be classified into passive (red points in Fig. 2), star-forming (blue points), and intermediate so-called green valley (green points) populations. The advantage of the NUVrK diagnostic over traditional single-colour classifications (e.g. $U-V$) is its ability to effectively disentangle the effects of dust extinction and star-formation activity on galaxy colours (Arnouts et al. 2013). This resolves the issue of dusty-red star-burst galaxies contaminating the red sequence passive population which plagues simpler ($U-V$)-type classifiers (e.g. Haines et al. 2008; Brammer et al. 2011).

There is good consistency between the classification of galaxies into blue cloud and red sequence populations from their d4000 value and that using the NUVrK diagnostic, at all stellar masses and redshifts covered by VIPERS. In the $0.50 < z < 0.65$ bin, 89% of NUVrK-selected passive galaxies have $d4000 > 1.55$, placing them along the red sequence in the d4000– M diagram, while 92% of NUVrK-selected star-forming galaxies have $d4000 < 1.55$ and lie along our blue sequence. Conversely, 95% of blue-cloud galaxies with $d4000 < 1.55$ would be classified as star-forming from their NUVrK colours. NUVrK-selected green valley galaxies share a similar distribution in the d4000– M plane to passive ones, and 72% have $d4000 > 1.55$.

An advantage of d4000 over the NUVrK diagnostic is that it provides a single continuous variable that can be readily associated to the mean stellar age or star-formation history of a galaxy (Kauffmann et al. 2003a; although see Arnouts et al. 2013, for how NUVrK colours can be used to estimate SFRs). This enables us to examine the distribution of d4000 values (or equivalently stellar ages), rather than simply split galaxies into two or three sub-populations. We seek to identify subtle changes in the d4000 values within sub-populations. These could be indicative

of ongoing changes within these populations owing to the slow decline of star-formation activity in normal blue-cloud galaxies at these redshifts, as well as the first stages of quenching that take a galaxy from the blue cloud to the red sequence. It also allows the properties of VIPERS galaxies at $0.5 < z < 1.0$ to be directly compared with those in the local Universe covered by the SDSS (Kauffmann et al. 2003a, 2006).

3.1. Evolution of the blue cloud since $z \sim 1$

Figure 1 allows the evolution of the blue cloud population to be followed in detail from $z = 1$ to the present day by carefully comparing the d4000 distributions at fixed stellar mass through the four redshift bins studied.

At $0.8 \leq z < 1.0$ (Fig. 1a), the $11.0 \leq \log_{10} M < 11.2$ stellar mass bin is the highest one in which the blue cloud can be defined. It appears as a flat shelf that extends over $d4000 \approx 1.3$ – 1.6 , which contains a significant fraction of the galaxy population in that mass bin. This shelf weakens through the next redshift bin, leaving nothing more than an extended tail of the red sequence by $0.5 \leq z < 0.65$ (Fig. 1c). The first feature which could be fitted as a blue cloud population at $0.5 \leq z < 0.65$ is the weak shelf at $d4000 \sim 1.4$ – 1.55 in the $10.8 \leq \log_{10} M < 11.0$ mass bin. In fact, the d4000 distribution of the 11.0 – 11.2 stellar mass bin at $0.80 < z < 1.0$, most closely matches that in the 10.8 – 11.0 mass bin at $0.65 < z < 0.80$ and the 10.6 – 10.8 mass bin (orange curve) at $0.50 < z < 0.65$. The upper stellar mass limit of the blue cloud appears to thus drop by ~ 0.3 dex from $M \sim 10^{11.2} M_{\odot}$ at $z \sim 0.90$ to $M \sim 10^{10.9} M_{\odot}$ by $z \sim 0.58$. An examination of Fig. 1d indicates that this mass limit drops by a further 0.2 dex up to the present day, the first signature of the blue cloud being the shelf that is apparent at $d4000 \sim 1.5$ – 1.7 in the 10.6 – 10.8 mass bin (orange curve).

This evolution of the blue cloud is summarized in Fig. 3, which plots the central d4000 values and 1σ widths of the blue cloud and the red sequence populations as a function of stellar mass for the four redshift bins discussed above. This shows that the location and extent of the blue cloud has evolved smoothly and continuously between $z \sim 1$ and the present day in two ways. First, the upper stellar mass limit of the blue cloud has

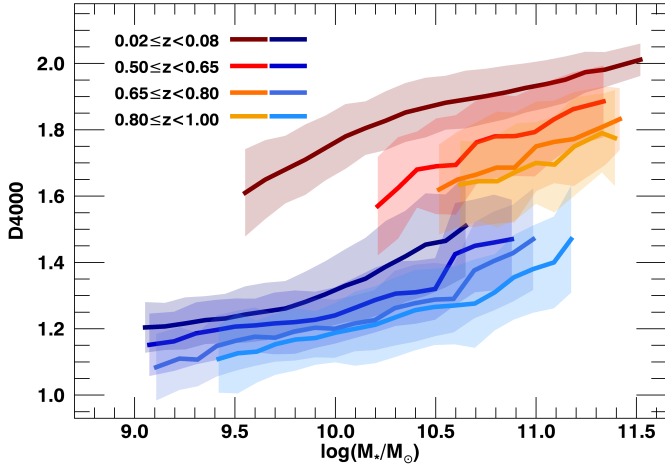


Fig. 3. Evolution of the blue cloud and red sequence in the d4000– M diagram from $z = 1.0$ to the present day. Each solid curve indicates the central d4000 value of the Gaussian fit to either the blue cloud or red sequence, as a function of stellar mass. The shaded regions indicate the 1σ widths of each Gaussian fit.

retreated steadily by ~ 0.5 dex from $\log_{10} M \sim 11.2$ at $z \sim 0.9$ down to 10.7 at $z \sim 0.06$, as described above. Second, the whole blue cloud has shifted to higher d4000 values at fixed stellar mass. For $M \lesssim 10^{10.5} M_{\odot}$, where the blue cloud has a Gaussian-like d4000 distribution, the central d4000 values increase by 0.05 – 0.07 between the 0.8 – 1.0 and 0.50 – 0.65 redshift bins, and another 0.07 – 0.10 by the present day. This gradual increase in d4000 with time probably reflects a combination of the steady $\sim 10\times$ decline in the specific-SFR (sSFR) of the star-forming main sequence between $z \sim 1$ and the present day (Noeske et al. 2007; Behroozi et al. 2013; Lee et al. 2015) and a slow ageing of their stellar populations over the intervening 8 Gyr.

In each redshift bin, the d4000– M relation for the blue cloud appears approximately linear with a slope of ~ 0.12 – 0.14 (with no sign of evolution), that starts to deviate from the linear approximation by turning upwards towards the high-mass limit. This upturn appears to initiate at ever lower stellar masses as time advances, from $M \sim 10^{10.7} M_{\odot}$ at $z \sim 0.9$ to $M \sim 10^{10.2} M_{\odot}$ by the present day.

3.2. Evolution of the red sequence since $z \sim 1$

The evolution of the red sequence from $z \sim 1$ to the present day shown by Fig. 3 can be summarized by two main changes. First, the red sequence as a whole has steadily shifted upwards to larger d4000 values with time, by ~ 0.12 between the 0.8 – 1.0 and 0.50 – 0.65 redshift bins, and a further ~ 0.13 up to the present day. The d4000– M relation appears roughly linear with a slope ~ 0.23 which does not vary within the VIPERS data, but flattens slightly to ~ 0.15 for the local SDSS dataset. The d4000– M relation for quiescent galaxies in VIPERS and its meaning in terms of the evolution of their stellar populations is beyond the scope of this paper, and is the focus of Siudek et al. (2017). Briefly, they argue that the slope of the relation is produced by increases in both age and metallicity with mass, with both effects of comparable importance. They also argue that the overall upwards shift of the d4000– M relation with time reflects the continual aging of the stars in these galaxies, but one that is slower than expected from a simple passive evolutionary model.

Second, while the red sequence already appears to be in place at the highest stellar masses at $z \sim 0.9$, it can be seen to extend

to ever lower stellar masses with time, reaching $M \sim 10^{9.6} M_{\odot}$ by the present day. For the $0.5 \leq z < 0.65$ redshift bin in particular, we confirm that our estimate of the lowest stellar mass at which the red sequence population can be identified with a peak or feature in the d4000 distribution ($M \sim 10^{10.2} M_{\odot}$) is robust against the effect of the $i_{AB} = 22.5$ VIPERS survey limit. We expect $\sim 90\%$ of red sequence galaxies at $M \sim 10^{10.2} M_{\odot}$ to have $i_{AB} < 22.5$.

Figure 1 shows that the stellar mass bins that first show a Gaussian-like d4000 distribution for the red sequence population are those at the highest stellar masses. Only the $M > 10^{11.2} M_{\odot}$ bin can be considered as being even marginally in place at 0.80 – 1.00 (Fig. 1a), while the first two mass bins ($M > 10^{11.0} M_{\odot}$) appear Gaussian-like at 0.65 – 0.80 (Fig. 1b), increasing to the top three mass bins ($M > 10^{10.8} M_{\odot}$) at $0.5 \leq z < 0.65$ (Fig. 1c). The finding of strongly-peaked d4000 distributions are indicative of relatively *mature* red sequence populations at these high stellar masses. Newly quenched galaxies (with d4000 ~ 1.6 – 1.7) arrive onto the sequence at a rate that is much lower than that when the bulk of the sequence was put in place. Instead, the stellar mass ranges where the d4000 distribution appears rather flat over 1.4 – 1.8 , should be those where the red sequence is *immature*, and being assembled at that redshift through the ongoing quenching of galaxies previously on the blue cloud. This can be seen occurring at $10.6 \leq \log_{10} M < 11.2$ at $0.8 \leq z < 1.0$ (Fig. 1a), $10.4 \leq \log_{10} M < 11.0$ at $0.65 \leq z < 0.80$ (Fig. 1b), and $10.2 \leq \log_{10} M < 10.8$ at $0.50 \leq z < 0.65$ (Fig. 1c). In other words, the stellar mass range where the red sequence is in the process of being assembled shifts steadily downwards with time.

3.3. Evolution in the transition mass of galaxies

One way of quantifying the effect of downsizing is to measure the transition mass, $M_{\text{cross}}(z)$, of galaxies as a function of redshift. This is defined as the stellar mass at which the number densities of blue cloud and red sequence galaxies are equal and their stellar mass functions intersect (Bundy et al. 2006; Davidzon et al. 2013). This indicates the transition from low-mass galaxies that are predominately star-forming to high-mass systems that are mostly quiescent (Kauffmann et al. 2003a).

For each redshift interval, we estimate the M_{cross} , where the number densities of blue cloud (d4000 < 1.55) and red sequence (d4000 > 1.55) galaxies are equal (Table 3), as shown in Fig. 4 by the solid red circles. The transition mass falls steadily with time within the VIPERS dataset from $\log_{10} M_{\text{cross}} = 10.99$ at $z = 0.90$ to $\log_{10} M_{\text{cross}} = 10.55$ at $z = 0.58$. The latter is very close to the $3 \times 10^{10} M_{\odot}$ value found by Kauffmann et al. (2003a) for local galaxies, suggesting little further evolution since $z \sim 0.5$. However, this oft-repeated value was only provided as a ballpark figure in Kauffmann et al. (2003a), where many global galaxy properties were seen to change. Applying the exact same threshold of d4000 = 1.55, we find $\log_{10} M_{\text{cross}} = 10.25$ or $1.76 \times 10^{10} M_{\odot}$ for SDSS galaxies with $0.02 \leq z < 0.08$ (red triangle). For comparison, Moustakas et al. (2013) obtain $\log_{10} M_{\text{cross}} = 10.33$ from their $0.01 \leq z < 0.20$ SDSS-GALEX sample.

The M_{cross} values from our VIPERS analysis are fully consistent with those produced by Vergani et al. (2008)³ applying a similar d4000 classification (red squares in Fig. 4) to galaxies in the VVDS (Le Fèvre et al. 2005). Their results indicate that the

³ After applying a -0.23 dex shift to correct the M_{cross} of Vergani et al. (2008) from a Salpeter IMF to the Chabrier IMF used here.

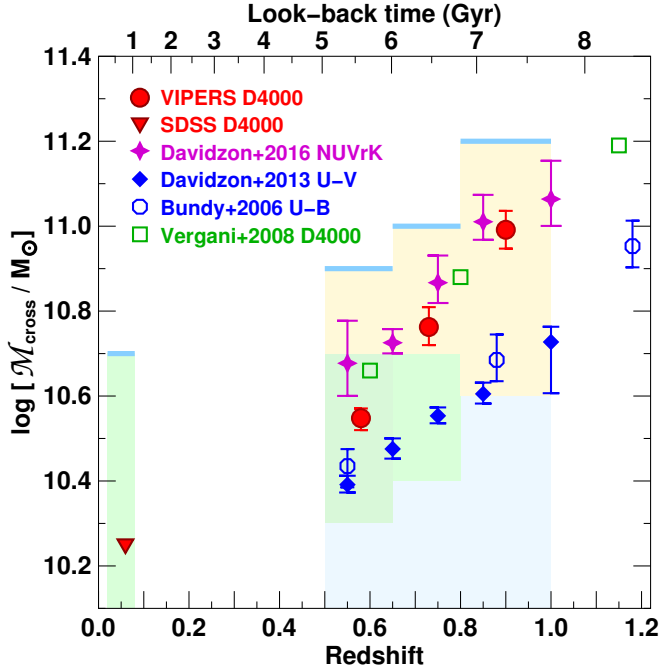


Fig. 4. Evolution of the transition mass $\mathcal{M}_{\text{cross}}$ as a function of redshift. Solid red symbols indicate the stellar masses where the number densities of blue cloud ($\text{d4000} < 1.55$) and red sequence ($\text{d4000} > 1.55$) galaxies are equal, with circles representing the three VIPERS bins and the triangle indicating $0.02 \leq z < 0.08$ SDSS galaxies. Solid symbols are based on VIPERS/SDSS data, while open points are $\mathcal{M}_{\text{cross}}$ values from the literature. Blue diamonds represent the $\mathcal{M}_{\text{cross}}$ values from Davidzon et al. (2013) using $U - V$ colour to classify blue and red galaxies, while magenta stars represent the $\mathcal{M}_{\text{cross}}$ values obtained applying the NUVrK classification of Davidzon et al. (2016) to the same VIPERS-PDR1 sample. The points from Vergani et al. (2008) are based on classification by D4000 break (green squares), and those from Bundy et al. (2006) are based on a $U - B$ classification (blue octagons). Light blue horizontal lines indicate the upper mass limit of the blue cloud (as in Fig. 3), pale yellow shaded regions indicate the stellar mass ranges where the d4000 distribution appears flat-topped, the pale green shaded regions indicate the stellar mass ranges where a green valley is apparent as a central dip in the d4000 distribution, while the light blue shaded regions are dominated by the blue cloud population.

transition mass keeps increasing steadily beyond $z \sim 1$, reaching $\mathcal{M}_{\text{cross}} = 10^{11.19} M_{\odot}$ at $z \sim 1.15$.

The transition masses presented here are systematically ~ 0.2 – 0.3 dex higher than those of Davidzon et al. (2013) who applied a $U - V$ classification to the VIPERS PDR1 sample (blue diamonds). However, when classifying galaxies using the NUVrK diagnostic of Davidzon et al. (2016), and reperforming the analysis on the same PDR1 sample, the resultant transition masses (magenta stars) and trends now appear rather consistent with those obtained using our d4000 classification. Bundy et al. (2006) split galaxies from the DEEP2 redshift survey by their $(U - B)$ colour, obtaining $\mathcal{M}_{\text{cross}}(z)$ values (open blue octagons) in agreement with those of Davidzon et al. (2013). The lower transition masses obtained when using optical colours to split galaxies could be due to the significant numbers of star-forming galaxies known to contaminate the red sequence owing to the effects of dust reddening (Haines et al. 2008; Brammer et al. 2011). This is supported by the $\mathcal{M}_{\text{cross}}(z)$ obtained using the NUVrK classifier being in much better agreement with those obtained using the d4000 spectral feature.

Table 3. Transition masses $\mathcal{M}_{\text{cross}}$ for our four redshift intervals.

Redshift	$\log(\mathcal{M}_{\text{cross}}/M_{\odot})$
0.02–0.08	10.246
0.50–0.65	$10.548^{+0.023}_{-0.028}$
0.65–0.80	$10.763^{+0.047}_{-0.043}$
0.80–1.00	$10.992^{+0.044}_{-0.044}$

To link these transition masses back to the d4000 distributions of Fig. 1, the upper stellar mass limits of the blue cloud determined in Sect. 3.1 are shown in Fig. 4 by blue horizontal lines. The steady fall in $\mathcal{M}_{\text{cross}}$ at least keeps pace (and may be more rapid) with the retreat of the upper stellar mass limit of the blue cloud since $z \sim 1$. For the upper reaches of the blue cloud at $0.5 \leq z < 1.0$, the d4000 distribution appears unimodal, with a flat top extending over d4000 values 1.4–1.8. The stellar mass bins where this flat-topped distribution is seen are shown in Fig. 4 by the yellow shaded regions. Interestingly, the lowest stellar mass where this behaviour is seen shows no evidence of evolving, remaining at $\sim 10^{10.7} M_{\odot}$. This is approximately the characteristic stellar mass $\mathcal{M}_{\text{SF}}^*$ obtained for the stellar mass function of star-forming galaxies, and which has been found to remain invariant at $\log_{10}(\mathcal{M}_{\text{SF}}^*) \sim 10.65$ over $0.0 \leq z \leq 1.5$ in numerous studies (e.g. Peng et al. 2010; Ilbert et al. 2013; Tomczak et al. 2014; Moutard et al. 2016b). This supports the view that $\mathcal{M}_{\text{SF}}^*$ marks the critical scale above which mass quenching becomes widespread (Bell et al. 2007). The stellar mass range where a green valley can be discerned as a central dip between relatively distinct red and blue sequences (green shaded region in Fig. 4), extends downwards from $\sim \mathcal{M}_{\text{SF}}^*$ to ever lower stellar masses with time, which parallels the evolution in $\mathcal{M}_{\text{cross}}$ and the high-mass limit of the blue cloud.

4. Evolution at the high-mass limit of the blue cloud

The previous section showed how the high-mass limit of the blue cloud has retreated from $\mathcal{M} \sim 10^{11.2} M_{\odot}$ at $z \sim 0.90$ to $\mathcal{M} \sim 10^{10.9} M_{\odot}$ by $z \sim 0.58$ and $\mathcal{M} \sim 10^{10.7} M_{\odot}$ up to the present day. How does this retreat (downsizing) translate into an evolution in the actual number density of massive galaxies?

Figure 5 plots the evolution in the number density of massive ($\mathcal{M} \geq 10^{11} M_{\odot}$) blue-cloud galaxies with $\text{d4000} < 1.55$ (blue points) over $0.50 \leq z < 1.0$. The volume covered by VIPERS is sufficient to contain over 1000 massive blue-cloud galaxies over this redshift range, allowing it to be finely divided into narrow redshift bins just 0.05 in width. Each galaxy is weighted by $(1/V_{\text{max}})(\text{TSR} \times \text{SSR})^{-1}$ to account for spectroscopic incompleteness. Table 4 reports the numbers of VIPERS galaxies in each redshift bin, and the resultant number density of massive blue-cloud galaxies. Based on their observed apparent i -band magnitudes, the loss of massive blue-cloud galaxies from the VIPERS survey as a result of being too faint ($i_{\text{AB}} > 22.5$) should be negligible, at least up to $z \sim 0.9$. We also do not expect to miss massive blue-cloud galaxies owing to the VIPERS $u - g$, $g - i$ colour selection criteria, since their observed colours remain reasonably far from the colour cuts used.

The number density of massive blue-cloud galaxies remains relatively constant at a value $\sim 8 \times 10^{-5} \text{Mpc}^{-3}$ over $0.75 \leq z < 1.0$, before rapidly dropping by a factor 4–5 over a time-scale of just ~ 1 Gyr, to reach a value of just $\sim 1.5 \times 10^{-5} \text{Mpc}^{-3}$ by $z \sim 0.6$. We find 342 massive blue-cloud galaxies within our

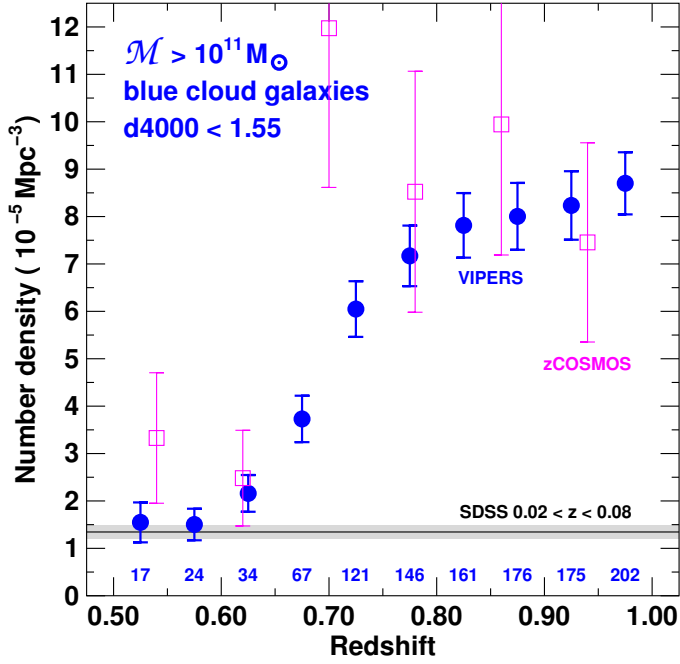


Fig. 5. Evolution in the number density of massive star-forming galaxies ($\mathcal{M} > 10^{11} M_{\odot}$ and $d4000 < 1.55$) from VIPERS (blue solid points) and the zCOSMOS 20K bright galaxy sample (magenta open squares) over $0.5 \leq z < 1.0$. The number of massive blue-cloud VIPERS galaxies in each redshift interval are indicated in blue. The black line and grey shaded region indicates the corresponding number density and 1σ confidence limits for the SDSS.

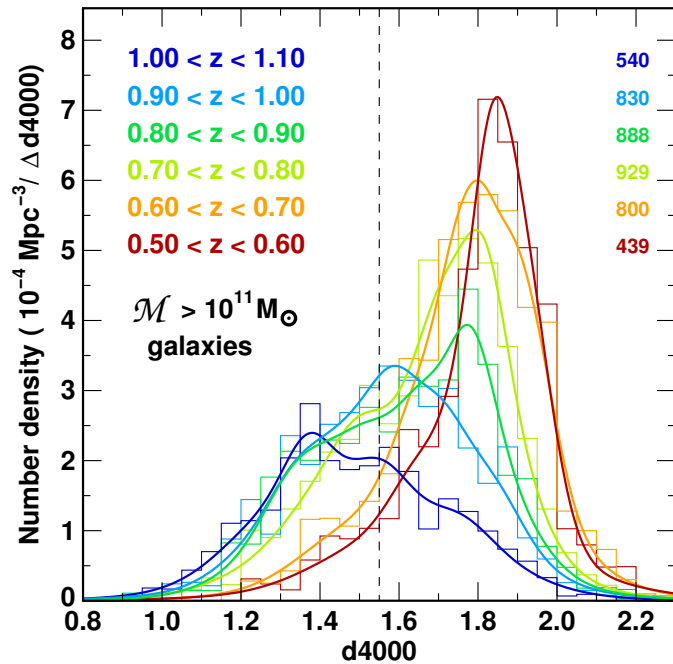


Fig. 6. Evolution of the d4000 distribution of massive galaxies. The curves are normalized to represent the number of $\mathcal{M} > 10^{11} M_{\odot}$ galaxies per unit comoving volume per unit d4000.

SDSS-DR7 subsample over $0.02 < z < 0.08$, corresponding to a number density of $1.34 \pm 0.15 \times 10^{-5} \text{ Mpc}^{-3}$ (black horizontal line). This suggests no further significant decline in the population after $z \sim 0.5$.

The sharp decline over $0.5 < z < 0.8$ is also seen in the zCOSMOS data (magenta squares), taken from the final

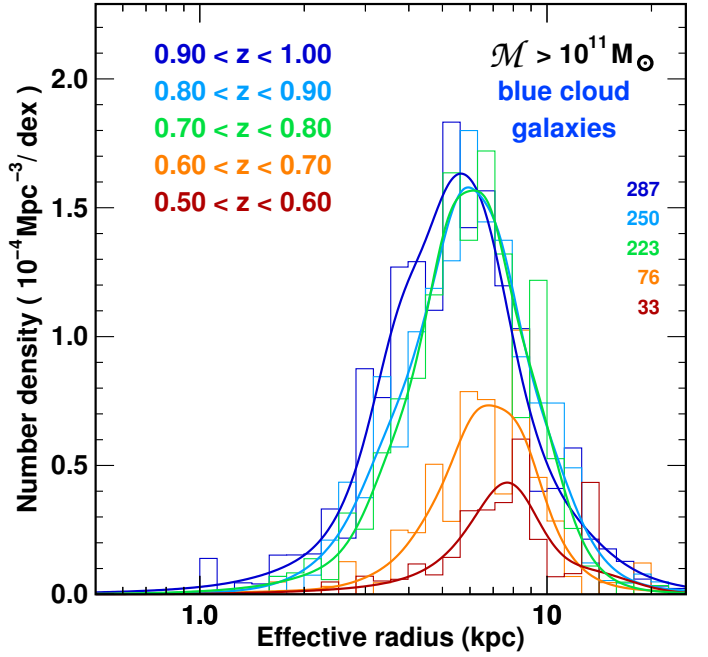


Fig. 7. Evolution in the size distribution of massive star-forming galaxies with $\mathcal{M} > 10^{11} M_{\odot}$ and $d4000 < 1.55$ over $0.5 \leq z < 1.0$, normalized per unit comoving volume per dex in r_e .

zCOSMOS-bright sample of about 20 000 galaxies over the 1.7 deg^2 COSMOS field and selected simply to have $I_{\text{AB}} \leq 22.5$ (Lilly et al. 2007, 2009), as measured from the COSMOS HST-ACS *F814W* images. Each galaxy is weighted to account for local spectroscopic incompleteness in the zCOSMOS survey in the same way as VIPERS. The smaller areal coverage means that cosmic variance effects are much more important for zCOSMOS, and the error bars include the expected bin-to-bin uncertainties that are due to cosmic variance (20–25% for our redshift bins of width 0.08), assuming the formula of Driver & Robotham (2010). The number densities seen in the three highest redshift bins in the zCOSMOS data are consistent with the high plateau seen in VIPERS, while the two lowest redshift bins show number densities $\sim 3\times$ lower, close to those seen in the much larger volume covered by VIPERS. The only inconsistency is seen in the bin centred at $z = 0.7$, which contains two previously known wall-like structures of connected groups at $z \sim 0.67$ and $z \sim 0.73$ (Knobel et al. 2012; Iovino et al. 2016) that dominate the number counts for this bin. The largest source of uncertainty in the evolution seen in the VIPERS data is unlikely to be Poisson noise or cosmic variance, but systematics in the stellar mass estimates. Moustakas et al. (2013) show that changing the stellar population synthesis models or the priors (e.g. the stochastic use of bursts) can affect the level of evolution observed in the number densities of massive star-forming galaxies (their Fig. 20). However, these effects do not appear large enough ($\lesssim 0.2$ dex over $0 < z < 1$) to fundamentally change our result.

Where have all these massive blue cloud galaxies gone? Assuming that they haven't lost any stellar mass, they must have left the massive blue cloud sample by becoming quiescent, increasing their d4000 values beyond our limit of 1.55. We investigate this in Fig. 6, which plots the d4000 distributions of $\mathcal{M} > 10^{11} M_{\odot}$ galaxies for six redshift bins spanning $0.5 \leq z < 1.1$, normalized per unit comoving volume. This figure encapsulates the wholesale shift in the d4000 distribution of the most massive galaxies over this period. These galaxies mostly lie

Table 4. Number density evolution of massive blue-cloud ($M > 10^{11} M_{\odot}$, $d4000 < 1.55$) galaxies in VIPERS.

Redshift range	$N_{\text{gals}} M > 10^{11} M_{\odot}$	$\rho_{\text{gals}} (10^{-5} \text{ Mpc}^{-3})$
0.50–0.55	17	1.55 ± 0.42
0.55–0.60	24	1.50 ± 0.33
0.60–0.65	34	2.16 ± 0.39
0.65–0.70	67	3.73 ± 0.48
0.70–0.75	121	6.05 ± 0.59
0.75–0.80	146	7.17 ± 0.64
0.80–0.85	161	7.81 ± 0.69
0.85–0.90	176	8.00 ± 0.69
0.90–0.95	175	8.23 ± 0.71
0.95–1.00	202	8.70 ± 0.65

within the blue cloud at $1.0 \leq z < 1.1$, peaking at $d4000 \sim 1.35$. This peak then shifts through intermediate values ($d4000 \sim 1.6$) in the next redshift slice ($0.9\text{--}1.0$) and onto the red sequence, which becomes gradually more dominant through to $z = 0.5$ as the blue cloud disappears. It is clear that the majority of the massive galaxies which resided in the blue cloud at $z \sim 1.1$ have been steadily transferring through the green valley and onto the red sequence by $z \sim 0.5$. These results are fully consistent with the systematic shifts in the $d4000$ distributions of $M > 10^{11} M_{\odot}$ galaxies from the VIMOS VLT Deep Survey (VVDS), with the median $d4000$ value shifting from 1.37 at $1.0 \leq z < 1.3$ to 1.69 at $0.5 \leq z < 0.7$ (Fig. 1 of Vergani et al. 2008).

Figure 7 presents the size distributions of these massive blue cloud ($M > 10^{11} M_{\odot}$, $d4000 < 1.55$) galaxies, for five redshift bins covering $0.5 \leq z < 1.0$, where size is quantified by the half-light radius, r_e , in kpc. The y axis indicates the number density of galaxies per unit comoving volume per dex in r_e , so that vertical shifts between curves reflect changes in the number density of blue-cloud galaxies of a fixed size. The highest three redshift bins are all consistent with a log-normal distribution of mean $r_e = 5.85$ kpc and 0.18 dex width, with no apparent changes in the number density at fixed size. As the overall number density drops sharply for the lowest two redshift bins, the mean proper effective radius rises to 7.39 kpc for $0.5 \leq z < 0.6$. The likelihood that a massive galaxy can remain on the blue cloud from $z \sim 0.8$ through to $z \sim 0.5$ depends strongly on its size. While the number density of massive blue-cloud galaxies that are more compact than average ($r_e < 5.85$ kpc) drops by a factor ten between $z \sim 0.8$ and $z \sim 0.5$, it falls by just a factor three for those galaxies larger than average. The mean size of these massive galaxies that must have left the blue cloud between $z \sim 0.8$ and $z \sim 0.5$ is 5.5 kpc.

In contrast, there is no sign of evolution in the Sérsic-index distribution of massive blue-cloud galaxies over this period, or a preferential quenching of these galaxies based on their structure. The distribution extends over $0.8 \leq \eta \leq 5.0$ (i.e. spanning both classical exponential and de Vaucouleurs profiles), peaking at $\eta \sim 2$ at all redshifts covered by VIPERS ($0.5\text{--}1.0$).

5. Evolution of the size-mass relation

We examine the evolution of the size-mass relation of galaxies from $z \sim 1$ to the present day in Fig. 8, plotting effective radius versus stellar mass for three redshift intervals: $0.7\text{--}1.0$, $0.5\text{--}0.7$ (VIPERS), and $0.02\text{--}0.08$ (SDSS). The VIPERS data are now split into just two redshift bins $0.7 \leq z < 1.0$ and $0.5 \leq z < 0.7$, which encapsulate the two phases of evolution seen in Fig. 5, and

span similar look-back times (1.41 and 1.26 Gyr, respectively). Galaxies are colour-coded by their $d4000$ values, enabling the dependence of a galaxy's star formation history on its size and stellar mass to be separated objectively, without a priori imposing a specific combination of the two properties (e.g. M/r_e , Σ_e). Black diagonal dashed lines mark constant inferred velocity dispersions of 100, 150, and 225 km s^{-1} assuming the relation $\sigma_{\text{inf}} = \sqrt{(0.3GM/r_e)}$ of Franx et al. (2008), where the constant was chosen so that the σ_{inf} of the SDSS galaxies matched the measured velocity dispersions (see also Bezanson et al. 2011).

Figure 8c shows $0.02 < z < 0.08$ galaxies from the SDSS-DR7 sample. Only galaxies identified as centrals by Yang et al. (2012) are plotted. Hence any trends should be due to the effects of mass quenching rather than environmental quenching that is due to the galaxy becoming a satellite within a more massive halo. Most notable is the fact that the galaxy population is very sharply bounded on three sides of the size-mass plot. There is an upper size limit of 10 kpc, rising slowly with stellar mass to 20 kpc by $M \sim 10^{11} M_{\odot}$, and a lower boundary at ~ 0.7 kpc (which may be a resolution limit). Most importantly, there is a very sharp upper stellar mass limit, which runs diagonally through the size-mass plot, approximately along the line of constant inferred velocity dispersion $\sigma_{\text{inf}} = 225 \text{ km s}^{-1}$. The empty region to the lower-right of this line is termed the zone-of-exclusion by Cappellari et al. (2013), as the region of the size-mass relation where none of their 260 local early-type galaxies from the ATLAS^{3D} survey are found. Taylor et al. (2010) warn that the absence of compact high-mass systems is at least partly due to SDSS spectroscopic target selection criteria, which exclude objects on the basis of having bright fiber magnitudes ($m_{\text{fib}} < 15$) to avoid cross-talk between the fibers. The SDSS should however be $>80\%$ complete for compact, massive galaxies at $z \gtrsim 0.06$.

It is immediately apparent that the star formation history of galaxies is also fundamentally defined by this same diagonal limit. Essentially all old, quiescent galaxies ($d4000 \gtrsim 1.8$; red points) are found within a narrow diagonal strip, some 0.5 dex wide in M , that runs parallel to this limit, confined between the two diagonal lines marking inferred velocity dispersions of 100 km s^{-1} and 225 km s^{-1} . In contrast virtually all galaxies to the left of these lines have young stellar populations with $d4000 \lesssim 1.4$ (green, blue points). These trends parallel those seen for local early-type galaxies within the ATLAS^{3D} survey, where their $g-i$ colours, H β absorption-line strengths, molecular gas fractions, SSP-equivalent stellar ages, metallicities, and abundances all follow trends of constant σ_{inf} in the size-mass plane (Cappellari et al. 2013; McDermid et al. 2015).

The VIPERS data allow the evolution of these sharp fundamental boundaries and behaviours to be followed back in time to $z \sim 1$ in comparable detail. The most notable aspect of Fig. 8 is the lack of difference in the basic distributions of galaxies in the size-mass plane at the three epochs. There are well-defined upper and lower size limits of ~ 1 kpc and 10 kpc in all three panels. The upper mass bound continues to run parallel to the lines of constant velocity dispersion, and the oldest galaxies with the highest $d4000$ values (red points) remain limited to a narrow diagonal band along this edge. While in the SDSS data, the most massive galaxies appear essentially confined just within the 225 km s^{-1} line, in the VIPERS data, some galaxies do appear to extend just beyond it (by up to 0.1–0.2 dex), suggesting a marginal shift since $z \sim 1$. The fundamental result of Fig. 8 appears that the basic properties of the size-mass relation were already in place at $z \sim 1$, and have only evolved gradually to the present day.

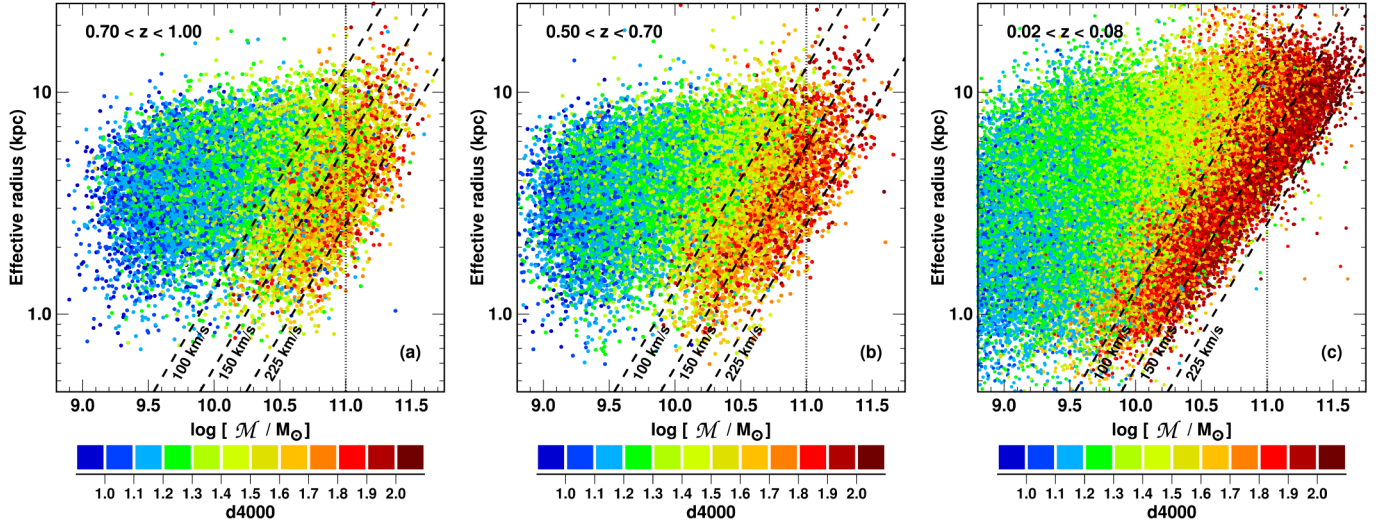


Fig. 8. Evolution of the size-mass relation of galaxies, plotting effective radius versus stellar mass for three redshift ranges: 0.70–1.00 (VIPERS), and 0.50–0.70 (VIPERS), and 0.02–0.08 (SDSS data). Each galaxy is colour coded according to its d4000 value as indicated in the colour bars *along the bottom*. Black diagonal dashed lines indicate lines of constant inferred velocity dispersion of 100, 150, and 225 km s^{−1} following [Franx et al. \(2008\)](#).

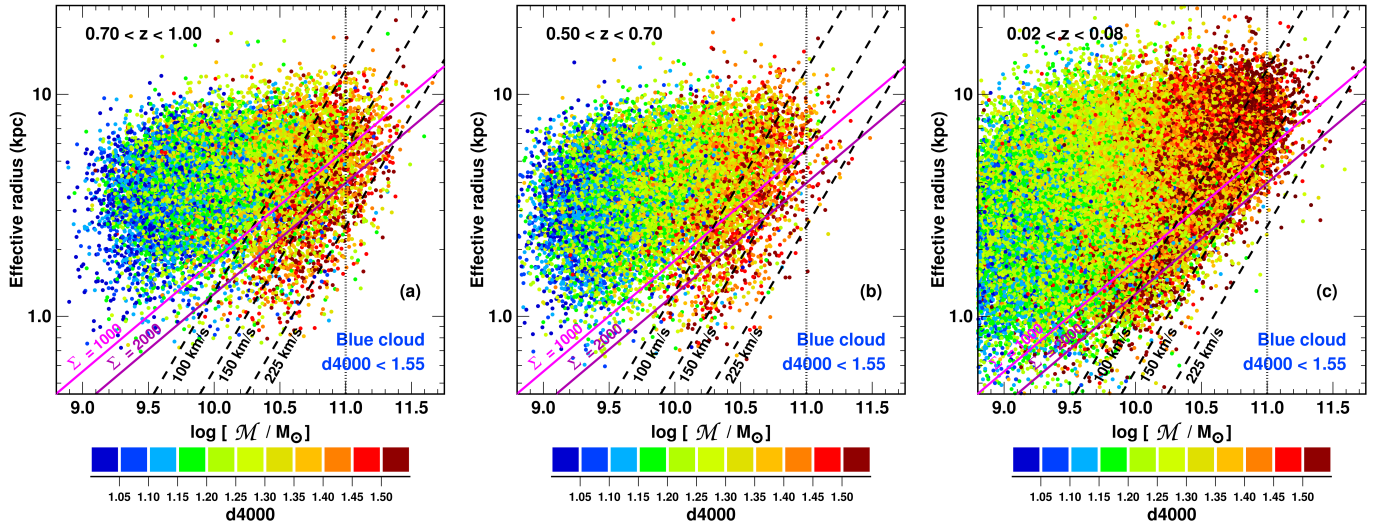


Fig. 9. Size-mass relation of blue-cloud galaxies ($d4000 < 1.55$), plotting effective radius r_e versus M for the same three redshift ranges as in Fig. 8: 0.7–1.0, 0.50–0.70 (VIPERS) and 0.02–0.08 (SDSS). Each galaxy is colour coded according to its d4000 index, as indicated in the colour bar *along the bottom*. Black dashed lines indicate inferred velocity dispersions of 100, 150, and 225 km s^{−1}. Magenta lines indicate effective stellar mass surface densities $\Sigma_e = 1000$ and $2000 M_\odot \text{pc}^{-2}$ as used in [Gargiulo et al. \(2016\)](#).

While the location of these massive quiescent galaxies in the size-mass plane appears to evolve little, moving to higher redshifts their d4000 values do appear to decline, which is indicative of younger stellar populations. The evolution of these massive, passive galaxies is the focus of [Gargiulo et al. \(2016\)](#), while in this work we explore what causes a star-forming galaxy at the upper end of the blue cloud to leave it and become quiescent. However, in Fig. 8, the upper-limits of the blue cloud and galaxies in the first stages of transformation are hidden, submerged under the dominant population of old, already quiescent galaxies.

5.1. The size-mass relation of blue-cloud galaxies

To gain insights into what processes push a galaxy from the upper end of the blue cloud, and fundamentally limit the ability of galaxies to continue to grow through star formation, Fig. 9 displays the size-mass relation for the same three redshift intervals

as Fig. 8, but plotting only blue-cloud galaxies ($d4000 < 1.55$). Galaxies are still colour-coded according to their d4000 index, but with a different scale to Fig. 8. The d4000 values of blue-cloud galaxies increase steadily with stellar mass, from ~ 1.1 (blue points) at the lowest masses to ~ 1.5 (red points) at the high-mass end. For stellar masses above $10^{10} M_\odot$ the dependence of d4000 appears tilted, such that smaller galaxies have slightly higher d4000 values at fixed stellar mass than larger ones. Moreover, the high-mass limit of the blue cloud appears tilted, such that it appears to run parallel to the diagonal black dashed lines marking constant inferred velocity dispersion σ_{inf} . For comparison, lines of constant stellar mass ($M = 10^{11} M_\odot$, dotted line) and stellar mass density Σ_e (magenta lines) run at significant angles with respect to the upper limit of the blue cloud.

There is evidence of evolution between the two highest redshift bins. At $0.7 \leq z < 1.0$ (Fig. 9a) the upper limit of the blue cloud is approximately demarcated by the final black dashed line

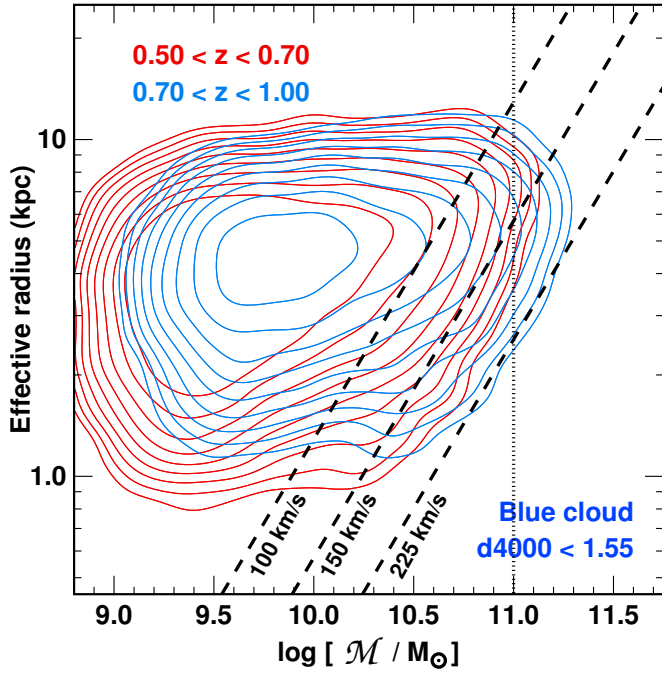


Fig. 10. Comparison of the bivariate number density distributions (per unit comoving volume) of effective radius (r_e) and stellar mass (M) for blue-cloud galaxies ($d4000 < 1.55$) in the two redshift ranges: 0.7–1.0 (blue contours) and 0.5–0.7 (red contours). Each contour indicates a factor $\sqrt{2}$ change in density.

at $\sigma_{\text{inf}} = 225 \text{ km s}^{-1}$, including a significant population with $M > 10^{11} M_{\odot}$. By $0.5 \leq z < 0.7$ (Fig. 9b), the upper limit of the blue cloud has now retreated to the middle black dashed line that indicates $\sigma_{\text{inf}} = 150 \text{ km s}^{-1}$, with just a smattering of points beyond it. This upper bound does not show signs of further movement to the present day (Fig. 9c), with blue-cloud galaxies from the SDSS-DR7 extending up to the $\sigma_{\text{inf}} = 150 \text{ km s}^{-1}$ dashed line, beyond which the number density drops abruptly.

The orange/red points in each panel indicate the galaxies on the high- $d4000$ wing of the blue cloud ($1.4 < d4000 < 1.55$). These are the galaxies that are most likely to be in the process of leaving the blue cloud, quench their star formation in the near future and become the next arrivals onto the red sequence. At all redshifts, these quenching galaxies lie within a diagonal band (0.6–0.7 dex wide in M) that runs parallel to the dashed lines of constant σ_{inf} . This tilted band extends over the full range of effective radii of the blue cloud population, indicating that blue cloud galaxies of all sizes are being quenched.

At $0.7 < z < 1.0$ (Fig. 9a), the quenching galaxies (orange/red points) appear mostly confined to the diagonal band between the first and third black dashed lines ($100 \leq \sigma_{\text{inf}} < 225 \text{ km s}^{-1}$). We call this diagonal region the quenching zone. A comparison to Fig. 8c shows that this quenching zone roughly corresponds to the region enclosing massive passive galaxies at the present day. Figure 9b indicates that, by $0.5 < z < 0.7$, most of those galaxies with $\sigma_{\text{inf}} > 150 \text{ km s}^{-1}$ must indeed have left the blue cloud, while those with $100 < \sigma_{\text{inf}} \leq 150 \text{ km s}^{-1}$ now represent the high-mass limit of the blue cloud and, having $d4000$ values ≥ 1.40 , are those most likely to leave in the near future. This changes little up to the present day (Fig. 9c).

For the SDSS galaxies (Fig. 9c) aperture effects may well cause the apparent extension of $1.4 < d4000 < 1.55$ galaxies to the left of the $\sigma_{\text{inf}} = 100 \text{ km s}^{-1}$ lines at large radii

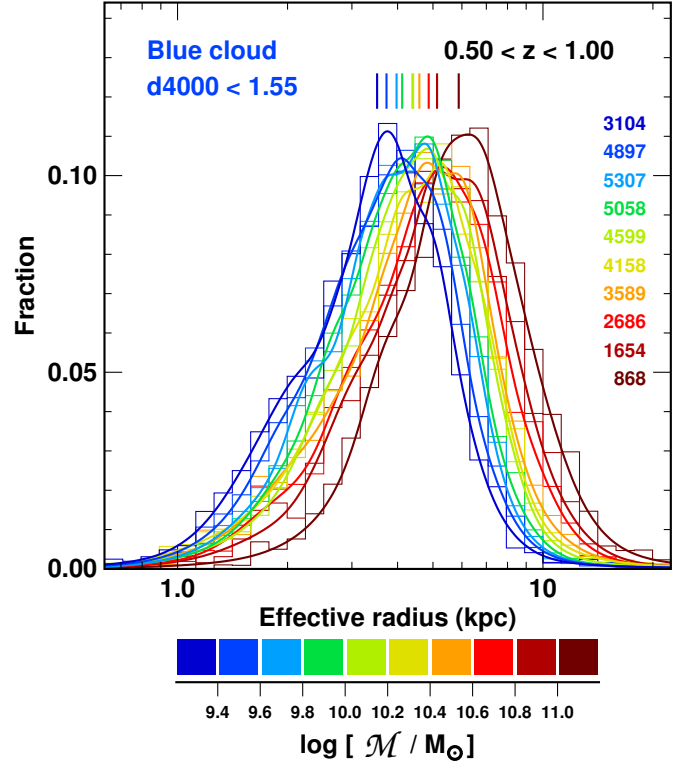


Fig. 11. Size distribution of blue cloud VIPERS galaxies ($d4000 < 1.55$, $0.5 \leq z < 1.0$) in ten 0.2 dex wide bins of stellar mass, colour coded as indicated. The median effective radius of blue-cloud galaxies in each stellar mass bin is indicated by the correspondingly coloured vertical line near the top.

($r_e \sim 10 \text{ kpc}$), since the $3''$ diameter (3.5 kpc at $z = 0.06$) SDSS fibres sample only inside $r_e/4$ for such large galaxies. The presence of a bulge component and steep negative metallicity gradients within disc galaxies could contribute to produce significant biases in the $d4000$ measurements of these objects (Kewley et al. 2005; González Delgado et al. 2015). At the redshift range of the VIPERS survey, the $1''$ slit-width corresponds to 6.1 kpc at $z = 0.5$ and 8.0 kpc at $z = 1.0$, and the slits are designed to be long enough to extend beyond the galaxy in both directions to measure the sky background (unlike fibres). We thus do not expect to be significantly affected by metallicity gradients, and note that they should act in the opposite direction to the observed trend.

Figure 10 directly compares the bivariate number density distribution of galaxies in the two highest redshift bins, weighting each galaxy to account for spectroscopic and stellar mass incompleteness, and accounting for the different comoving volumes sampled by VIPERS over the two redshift ranges. The high-mass limit of the blue cloud at $0.7 \leq z < 1.0$ (blue contours) is shifted 0.17 dex to higher stellar masses with respect to that at $0.5 \leq z < 0.7$ (red contours) at fixed effective radius. The iso-density contours along this high-mass edge are parallel to the dashed lines for both redshift bins, confirming that the upper limit of the blue cloud runs along lines of constant M/r_e . The retreat in the blue cloud revealed in Fig. 10 appears to be systematic, with no significant dependence on effective radius. This suggests that the size distribution of galaxies leaving the blue cloud is similar to that of galaxies that are still in it.

Figure 11 shows how the size distribution of blue cloud galaxies varies as a function of stellar mass, averaged over the combined VIPERS redshift range ($0.5 \leq z < 1.0$). The curves

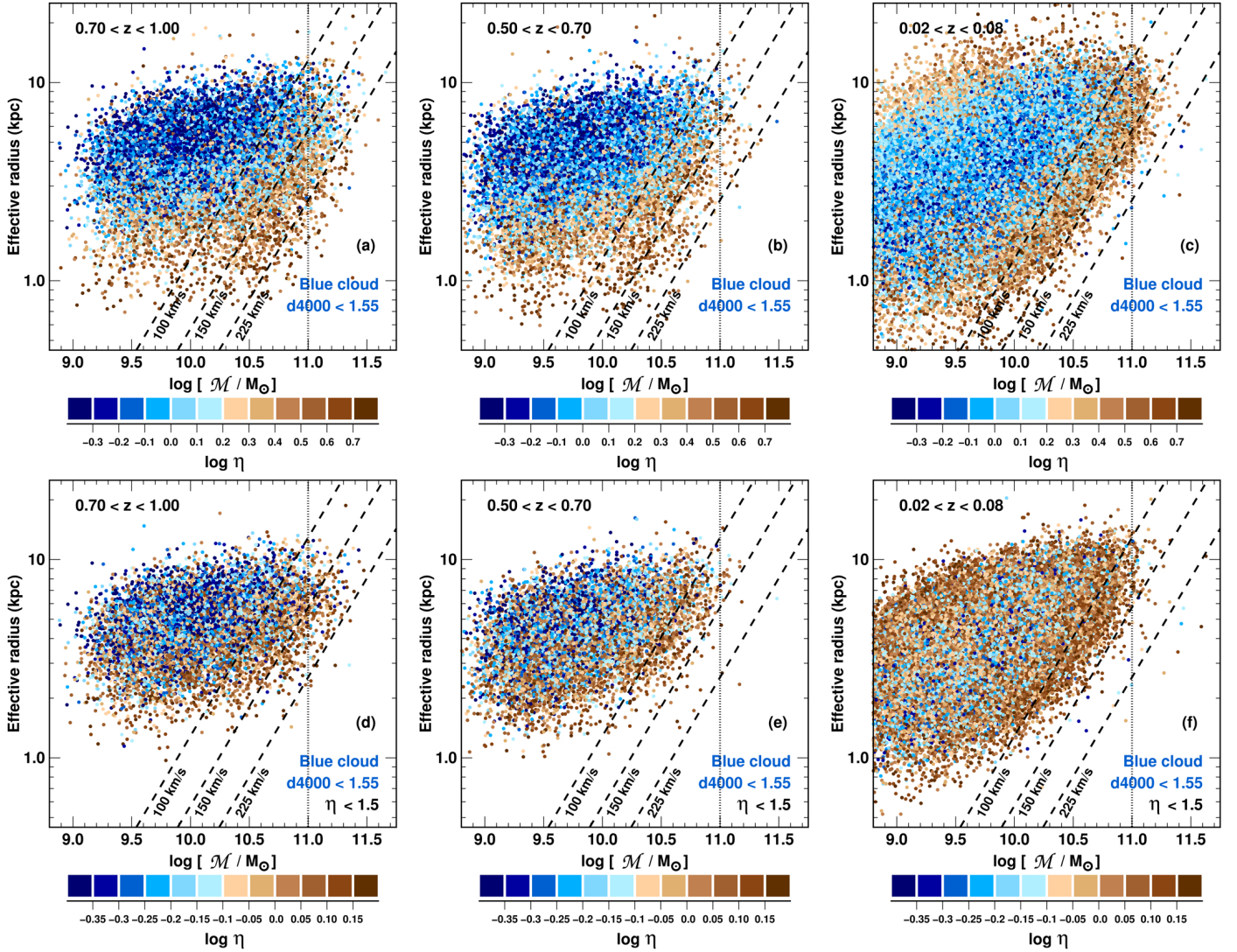


Fig. 12. Size-mass relation of blue-cloud galaxies ($d4000 < 1.55$), plotting effective radius r_e versus M for three redshift ranges (*upper panels*): 0.7–1.0, 0.5–0.7 (VIPERS) and 0.02–0.08 (SDSS). Galaxies are colour coded according to their Sérsic index, as indicated in the colour bar *along the bottom*. Blue points indicate late-type galaxies ($\eta < 1.5$) while brown points are early-types. The three *lower panels* show the same size-mass relations, but plotting only classic late-type galaxies with $\eta < 1.5$.

plot the fraction of blue-cloud galaxies as a function of the logarithm of the half-light radius r_e in ten 0.2 dex wide stellar mass bins. The size distributions for all mass bins can be well described by a log-normal function, with a width of 0.20 dex that does not vary with mass. This is fully consistent with the log-normal size distribution and widths seen by Kauffmann et al. (2003a) for local galaxies at fixed stellar mass, confirming that this behaviour holds out to $z \sim 1$. While the shape and width of the size distribution of blue-cloud galaxies shows no dependence on stellar mass, the whole distribution gradually shifts to larger radii with stellar mass, such that the median half-light radius increases as $r_{e,\text{med}} \propto M^{0.10}$.

In classical models of disk galaxy formation, angular momentum is expected to be approximately conserved as the gas collapses to form the disk, such that the specific angular momentum of the resultant disk should be similar to that of its hosting dark matter halo (Fall & Efstathiou 1980; Mo et al. 1998). The characteristic radius of the disk R_d should then scale as $R_d \propto \lambda R_{\text{halo}}$, where R_{halo} is the virial radius of the DM halo, and λ is the dimensionless spin parameter, quantifying the DM halo’s angular momentum. N -body simulations have shown that the

spin parameter also shows a log-normal form with $\langle \lambda \rangle \simeq 0.035$ and $\sigma_\lambda \sim 0.20$ –0.25 dex (Macciò et al. 2008; Zjupa & Springel 2017). The log-normal size-distribution of star-forming galaxies observed here and in the local Universe thus remain in remarkable agreement with predictions of this simple theoretical model.

5.2. Changes in galaxy structure within the blue cloud

The upper panels of Fig. 12 plot the size-mass relation of blue cloud galaxies ($d4000 < 1.55$) for three different redshift intervals as before, but now colour code galaxies according to their Sérsic index η , rather than $d4000$ value. The first two panels show that the concentrations (η) of blue cloud galaxies within VIPERS ($0.5 \leq z < 1.0$) vary systematically with size and stellar mass in two different directions. First, for galaxies to the left of the $\sigma_{\text{inf}} = 100 \text{ km s}^{-1}$ line, their Sérsic index increases steadily as galaxies become smaller, from $\eta \lesssim 1.0$ for larger galaxies with $r_e \gtrsim 3 \text{ kpc}$, to $\eta \gtrsim 2.5$ for the most compact systems with $r_e \lesssim 2 \text{ kpc}$, and little additional dependence on stellar mass. Second, the Sérsic index also increases with stellar mass, with the $\sigma_{\text{inf}} = 100 \text{ km s}^{-1}$ line dividing low-mass galaxies

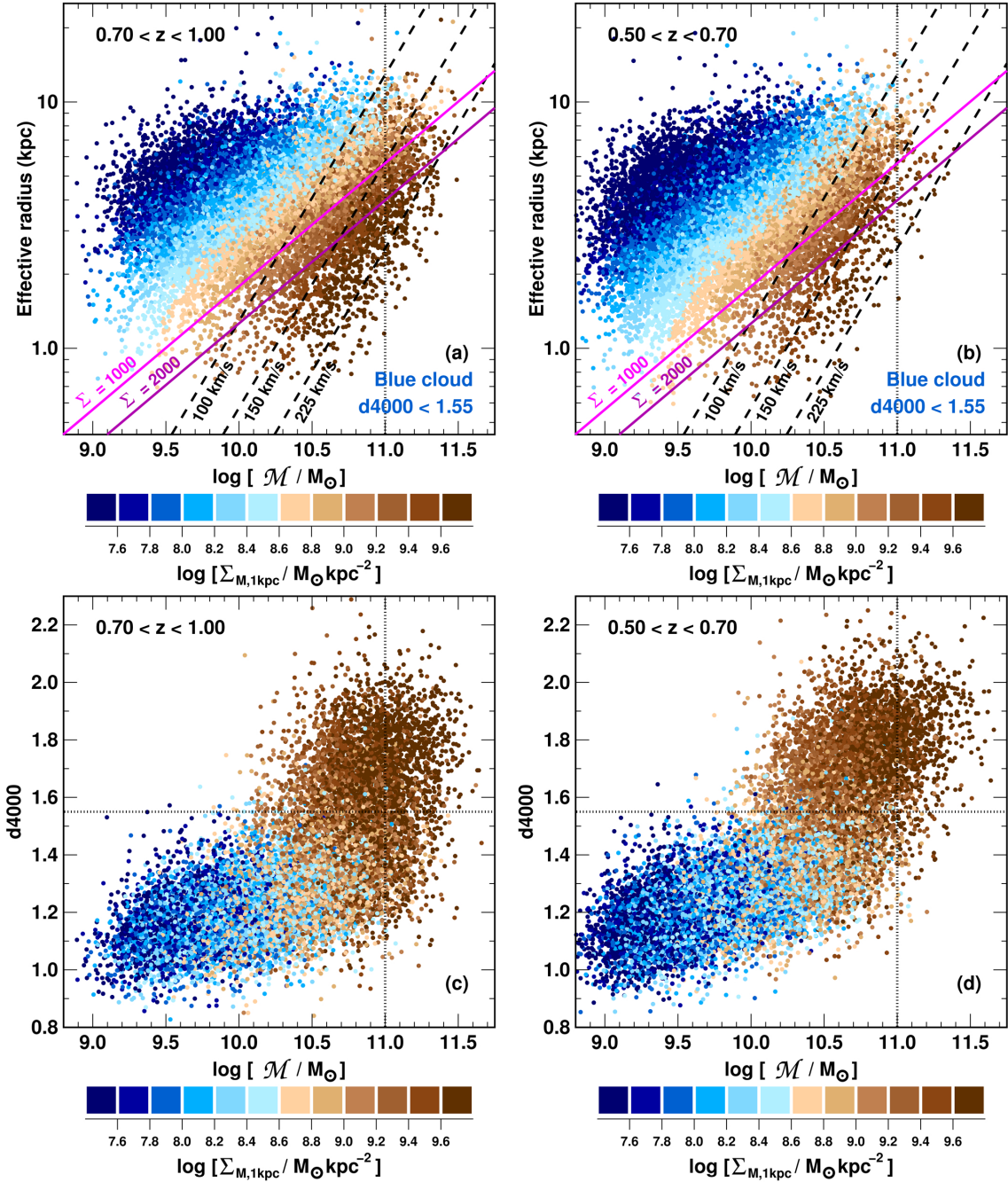


Fig. 13. Impact of central stellar mass surface density Σ_1 . The *top panels* plot the size-mass relation of blue-cloud galaxies for the redshift bins, $0.7-1.0$ and $0.5-0.7$, colour coded according to central stellar mass surface density Σ_1 , as indicated in the colour bar *along the bottom*. The *lower panels* plot the $d4000$ versus stellar mass relation for VIPERS galaxies for the same two redshift bins, again colour coded by Σ_1 . Horizontal and vertical dotted lines indicate the $d4000 = 1.55$ divider and $\log M = 11.0$ mass limit.

with late-type morphologies ($\eta < 1.5$, blue points) and high-mass systems with increasingly concentrated profiles, reaching $\eta \gtrsim 2.5$ (brown points) for those galaxies on the high-mass edge of the blue cloud. This latter trend parallels that seen for $d4000$ in Figs. 9a, b for the same blue-cloud galaxies. As galaxies in the blue cloud start to approach its high- σ_{inf} edge, both their internal structures and their ability to continue forming stars are being systematically affected, even as they remain within the blue cloud. In contrast, no such change in $d4000$ values is seen for the compact low-mass systems to parallel the increase in η .

The lower panels show that these same trends are apparent, even when considering only morphologically-secure late-type galaxies with $\eta < 1.5$. That is, the late-type galaxies with

the highest σ_{inf} ($>100 \text{ km s}^{-1}$), also have the highest Sérsic indices ($1.0 \lesssim \eta < 1.5$, brown points), while those to the left of the 100 km s^{-1} line have $\eta \lesssim 1.0$ (blue points). Even the first phases of structural transformation are aligned with an increase in σ_{inf} . The regions where late-type galaxies on the blue cloud can appear on the size-mass plane can be seen to have shrunk considerably in Figs. 12d, e from the upper panels where no morphological selection was made. First, all of the most compact galaxies ($\lesssim 1.5 \text{ kpc}$) have disappeared, reducing the overall radial (vertical) extent of the blue cloud at all stellar masses. Second, and more importantly, the high-mass limit appears to have retreated by $0.10-0.15 \text{ dex}$. Only 30% of $\sigma_{\text{inf}} > 100 \text{ km s}^{-1}$ blue-cloud galaxies at $0.5 < z < 0.7$ have $\eta < 1.5$. This shrinkage

demonstrates the comprehensive nature of the physical processes that are driving the structural changes in blue cloud galaxies in certain regions of the size-mass plane.

As before, the SDSS-DR7 dataset can be used to see whether the patterns apparent in the size-mass relation of blue-cloud galaxies at $0.5 \leq z < 1.0$ remain to the present day. Figure 12c confirms that $0.02 \leq z < 0.08$ blue cloud galaxies are confined to the same regions of the size-mass plane as VIPERS galaxies at $0.5 \leq z < 0.7$. The high-mass limit of the blue cloud at $z \sim 0$ essentially runs along the line marking $\sigma_{\text{inf}} = 150 \text{ km s}^{-1}$. The connections between morphology (η) and location of a galaxy in the size-mass plane are also persistent. Low-mass galaxies with $\sigma_{\text{inf}} < 100 \text{ km s}^{-1}$ are virtually all late types ($\eta < 1.5$; blue points), except for the most compact ($r_e \lesssim 1.5 \text{ kpc}$) and large systems ($r_e \gtrsim 10 \text{ kpc}$) which show higher concentrations. As blue-cloud galaxies push through the $\sigma_{\text{inf}} = 100 \text{ km s}^{-1}$ line and approach the high-mass boundary of the blue cloud population, their structures become increasingly concentrated ($\eta > 2$; brown points). Repeating this analysis using the bulge-to-total ratios of Simard et al. (2011) produces the same global trends (Appendix B). Galaxies on the leading edge of the blue cloud have significant bulge components ($0.3 \lesssim (B/T) \lesssim 1.0$), while lower mass systems are uniformly disc-dominated ($B/T < 0.25$).

5.3. The link to central stellar mass surface density

Numerous studies have indicated that the central stellar mass surface density Σ_1 is a much better predictor of star formation activity within a galaxy than stellar mass (Cheung et al. 2012; Fang et al. 2013; Barro et al. 2017; Whitaker et al. 2017), while the presence of a prominent bulge appears a necessary condition for galaxies to quench star formation on galaxy-wide scales (Bell 2008; Bell et al. 2012). However, while the results presented above show clear trends that connect the changes in d4000 and η with the location of galaxies in the size-mass relation, and in particular along lines of constant M/r_e or σ_{inf} , it is not clear how these trends relate to Σ_1 .

Figure 13a shows the variation of central stellar mass surface density Σ_1 within the size-mass plot for blue-cloud galaxies, over the redshift interval $0.7 \leq z < 1.0$. The Σ_1 values can be well described as a function of just size and mass, with little scatter in Σ_1 among galaxies of a fixed size and mass. Overall, the Σ_1 values increase from the top-left of the plot (large low-mass galaxies) towards the lower-right (compact massive galaxies), as expected for a density measure. The iso- Σ_1 contours notably change slope through the plot, from being parallel to lines of constant Σ_e (magenta lines) for $\log_{10}\Sigma_1 \lesssim 8.6$ (blue points), then gradually becoming steeper to become parallel to lines of constant σ_{inf} (black dashed lines) for the highest central stellar mass densities ($\log_{10}\Sigma_1 \gtrsim 9.2$; darker brown points). As a result, the upper limit of the blue cloud could also be defined as a threshold in Σ_1 , as well as σ_{inf} (or M/r_e). A comparison to the same size-mass plot for $0.5 \leq z < 0.7$ blue-cloud galaxies (Fig. 13b) shows that the retreat of the high-mass limit of the blue cloud revealed in Fig. 9 can be explained as the selective removal of those galaxies with the highest central stellar mass densities ($\log_{10}\Sigma_1 \gtrsim 9.4$; dark brown points).

Figures 13c and d show the distributions of VIPERS galaxies in the d4000– M plane for the same two redshift intervals ($0.7\text{--}1.0$ and $0.5\text{--}0.7$), colour coded by Σ_1 . In both panels, quiescent galaxies ($d4000 > 1.55$) uniformly have high central stellar mass densities, $\log_{10}\Sigma_1 \gtrsim 9.0$ (brown points). In the transition mass regime ($10.2 < \log_{10}M < 11.0$) where both blue cloud and red sequence galaxies co-exist, those galaxies with low central

stellar mass densities $\log_{10}\Sigma_1 < 8.6$ (blue points) are confined within the blue cloud. Within the blue cloud population, Σ_1 increases linearly with stellar mass, albeit with significant scatter, such that all massive blue-cloud galaxies with $M > 10^{11} M_\odot$ also have high central stellar mass densities ($\log_{10}\Sigma_1 \gtrsim 9.0$; brown points), for both redshift intervals. Thus, the massive blue cloud galaxy population ($M > 10^{11} M_\odot$) at $0.7 < z < 1.0$, many of which must leave the blue cloud and be quenched by $z \sim 0.5$ (Fig. 5), already have the high Σ_1 values that are seemingly a prerequisite for this quenching process to commence.

6. Discussion

In Fig. 1, we plotted the d4000 distributions of galaxies as a function of mass and redshift, revealing how the bimodal d4000 distribution seen among galaxies in the local Universe has developed over the last eight billion years. This enabled us to track the evolution of the location and extent of both the blue cloud and red sequence in the d4000– M plane (Fig. 3). This revealed how the high-mass limit of the blue cloud has retreated significantly, from $M \sim 10^{11.2} M_\odot$ at $z \sim 0.9$ to $M \sim 10^{10.7} M_\odot$ by the present day. This retreat is what Cowie et al. (1996) referred to when coining the term “downsizing”.

This observed downsizing of star formation can be understood by considering the recent findings that the SFR– M relation of the main sequence of star-forming galaxies is not linear ($\text{SFR} \propto M$) throughout as previously thought (Elbaz et al. 2007; Peng et al. 2010), but shows a clear flattening at high masses (Whitaker et al. 2014; Lee et al. 2015; Tomczak et al. 2016). The curvature of the SFR– M relation increases with time, while the stellar mass at which the sequence starts to bend downwards decreases with time (Lee et al. 2015). This means that the rate of decline in the SFRs of blue-cloud galaxies is much greater at the highest masses ($M \gtrsim 10^{11} M_\odot$), than at lower masses ($M \lesssim 10^{10} M_\odot$) where the relation is still close to linear.

We model the mass growth and sSFR evolution of star-forming galaxies for a range of final stellar masses (see Appendix C for details), assuming that blue-cloud galaxies assemble their stellar mass through star formation, at rates following the evolving SFR– M relation of star-forming galaxies from Tomczak et al. (2016), and taking into account stellar mass loss following Moster et al. (2013). This shows how the overall star-formation history and stellar mass assembly (through star formation) is accelerated in the most massive blue-cloud galaxies relative to their lower-mass counterparts (Fig. C.1). Notably, the stellar mass at which the sSFR of blue-cloud galaxies is equal to $1/t_0(z)$, where $t_0(z)$ is the age of the Universe at redshift z , is very close to the high-mass limits of the blue cloud that we obtain over $0 < z < 1$. At $z = 0.8$, the stellar mass of blue-cloud galaxies where $\text{sSFR} = 1/t_0$ is $M = 10^{11.10} M_\odot$, falling to $M = 10^{10.55} M_\odot$ by $z = 0$ (Fig. C.1b). As d4000 can be considered a proxy for sSFR, it seems plausible that as the sSFRs of massive blue-cloud galaxies decline steadily with time, their d4000 values correspondingly rise and eventually cross our $d4000 = 1.55$ threshold, taking them out of our blue cloud sample.

6.1. The decline of massive star-forming galaxies and the rise of massive passive galaxies

Figure 5 shows how the number density of massive blue-cloud galaxies ($M > 10^{11} M_\odot$, $d4000 < 1.55$) rapidly dropped five-fold between $z \sim 0.8$ and $z \sim 0.5$. This result appears surprising given the consensus view that the SMF of star-forming galaxies

has not changed significantly since $z \sim 1.3$ (Borch et al. 2006; Bell et al. 2007; Vergani et al. 2008; Pozzetti et al. 2010). But these papers were based on surveys covering $\sim 1 \text{ deg}^2$ and thus strongly affected by cosmic variance. More recently, Moustakas et al. (2013) again find no evolution over $0 < z < 1$ in the SMF of star-forming galaxies at intermediate masses ($10^{9.5} - 10^{11} M_\odot$) within the 5.5 deg^2 PRIMUS survey. However, they also find that the number density of the most massive star-forming galaxies ($M > 10^{11} M_\odot$) declines by 55% since $z \sim 1$. Brammer et al. (2011) observe an overall $\sim 4\times$ decline in the number densities of $M > 10^{11} M_\odot$ UVJ-selected star-forming galaxies between $z = 1.9$ and $z = 0.6$. Chen et al. (2012) report that the fraction of extremely massive galaxies ($M > 10^{11.4} M_\odot$) with significant recent star formation has fallen $\sim 4\text{--}10\times$ since $z \sim 0.6$, while Davidzon et al. (2013) find that the number density of such extremely massive ($M > 10^{11.4} M_\odot$) blue galaxies drops markedly between $z \sim 0.8$ and $z \sim 0.6$.

Figure 6 shows that these massive blue-cloud galaxies are being steadily quenched throughout this period ($0.5 < z < 1.0$), transferring from the blue cloud to the red sequence. Using the exact same stellar mass limit as applied here, Gargiulo et al. (2016) select massive galaxies with $M > 10^{11} M_\odot$ from the same VIPERS PDR-2 sample, and split them into star-forming and passive using the NUVrK selection of Davidzon et al. (2016). They find that the overall number density of massive passive galaxies has increased steadily from $9.7 \pm 0.3 \times 10^{-5} \text{ Mpc}^{-3}$ at $z = 0.95$ to $16.1 \pm 0.4 \times 10^{-5} \text{ Mpc}^{-3}$ at $z = 0.60$, while the number density of massive star-forming galaxies drops over the same period. Indeed, they confirm that the growth in the abundance of massive passive galaxies can be fully accounted for by the corresponding decline in massive (NUVrK-selected) star-forming galaxies. The increase in the number density of massive passive galaxies observed by Gargiulo et al. (2016) is also fully consistent with the decline in the number density among the massive blue-cloud population (d4000-selected) from $8.2 \pm 0.7 \times 10^{-5} \text{ Mpc}^{-3}$ at $z = 0.95$ to $1.5 \pm 0.3 \times 10^{-5} \text{ Mpc}^{-3}$ by $z \sim 0.6$ reported in our Fig. 5.

Gargiulo et al. (2016) split the massive passive galaxies (MPGs) according to their mean stellar mass density Σ_{r_e} , and find that while the densest MPGs ($\Sigma_{r_e} > 2000 M_\odot \text{ pc}^2$; below the lower magenta line in Fig. 9) show essentially no evolution in number density, the least dense MPGs ($\Sigma_{r_e} < 1000 M_\odot \text{ pc}^2$; above the higher magenta line in Fig. 9) show very rapid evolution in their number density, that can explain most of the global increase in number density of MPGs.

6.2. The size-mass relation

Figure 8 shows that the distribution of galaxies in the size-mass plane were confined to specific regions, with effective radii in the range $\sim 1\text{--}10 \text{ kpc}$, and an upper mass limit that runs diagonally in the plots approximately along lines of constant M/r_e or inferred velocity dispersion. These fundamental boundaries evolve little over $0 < z < 1$, except that at fixed mass, high-mass systems may be slightly more compact at $0.7 \leq z < 1.0$ than seen in the local Universe.

In all three redshift bins, old, red sequence galaxies with $d4000 \gtrsim 1.8$ lie within a narrow, diagonal band that runs parallel to this fundamental high-mass limit for galaxies. The dependence of $d4000$ appears tilted, so that galaxies with the same $d4000$ value lie along lines of constant velocity dispersion (dashed lines). Shetty & Cappellari (2015) find similar trends

for SSP-equivalent stellar ages following constant velocity dispersion for a sample of 154 galaxies at $0.7 < z < 0.9$, comprising both star-forming and quiescent galaxies. Whitaker et al. (2017) examined the relationships between specific SFR (sSFR; based on stacking analysis of *Spitzer*/MIPS $24 \mu\text{m}$ photometry) and the location of galaxies within the size-mass plane for $0.5 < z < 2.5$ galaxies from the CANDELS and 3D-HST surveys. They obtain very similar trends to those seen in Fig. 8, with specific-SFR decreasing with stellar mass, such that galaxies along lines of constant M/r_e have the same specific-SFRs. These trends are seen in all three of their redshift bins: $0.5\text{--}1.0$, $1.0\text{--}1.5$, and $1.5\text{--}2.5$.

Using SDSS-DR7 data, Omand et al. (2014) examined how the fraction of quiescent (defined using a cut in sSFR) galaxies (f_Q) depends on size (r_e) and stellar mass. For central galaxies, they find a sharp transition from mostly active galaxies to mostly quiescent, with contours of constant f_Q that approximately follow $M \propto r_e^{1.5}$. Among the actively star-forming galaxies, the sSFRs show a significant dependence on effective radius at fixed stellar mass, being ~ 0.2 dex lower for more compact systems, at least at intermediate masses ($10^{10} \leq M < 10^{11} M_\odot$).

Lilly & Carollo (2016) caution us not to overinterpret the trends shown in Fig. 8, or those of Omand et al. (2014), as proof that changes in galaxy structure must be associated with the quenching process. They point out the simple observation that star-forming galaxies have undergone continual size-growth at fixed instantaneous stellar mass of the form $r_e \propto (1+z)^{-1}$ since $z \sim 6$ (Buitrago et al. 2008; Newman et al. 2012; Mosleh et al. 2012; Patel et al. 2013; van der Wel et al. 2014). Hence galaxies that formed their stars earlier (have larger $d4000$ values) will naturally be smaller than those of the same stellar mass whose stars formed later, without any need for structure-dependent quenching processes. Likewise, quiescent galaxies at any epoch will be smaller than star-forming galaxies of the same stellar mass, since the star-forming progenitors of the quiescent galaxies would have been much smaller at the epoch at which they ceased forming stars. Lilly & Carollo (2016) consider a toy model for the growth of star-forming galaxies in which the radial distribution of new stars being formed within the galaxy always follows an exponential profile with a scale length $r_{e,\text{SF}} \propto M(z)^{1/3} (1+z)^{-1}$, while their specific SFRs evolve to match observations of the main star-forming sequence. This naturally ensures that ongoing star formation is always more radially extended within these star-forming galaxies than the integrated radial distribution of stars formed previously (as observed; Nelson et al. 2016), resulting in inside-out growth. For the most massive star-forming galaxies ($> M_{\text{SF}}^*$) central dense concentrations (bulges) are produced with $\Sigma_1 > 10^9 M_\odot \text{ pc}^{-2}$, owing to the stars formed at early epochs when the galaxy was much smaller. Steep positive radial gradients in sSFR are also naturally produced, similar to those seen in massive star-forming galaxies at $z \sim 2$ (Tacchella et al. 2015).

Lilly & Carollo (2016) show that a quenching mechanism that terminates star formation in the model galaxies with a likelihood that depends solely on their stellar mass (and not structure), can result in iso-quenched fraction contours among central galaxies that lie along lines of constant surface density Σ_{r_e} , closely reproducing the observations of Omand et al. (2014). Omand et al. (2014) also show that such trends can also be produced by a quenching mechanism that depends only on M , but which also reduces the galaxy size r_e by a factor two. Finally, the sizes and masses of already quenched galaxies can change significantly over time as the result of dry mergers and repeated minor merging (van Dokkum et al. 2010; Cappellari et al. 2013),

further altering the patterns of f_Q within the size-mass plane. All the above processes can thus artificially create or alter apparent trends seen in Fig. 8 or in f_Q over the size-mass plane.

We thus argue that to determine the relevance of galaxy structure in terminating star formation in blue-cloud galaxies requires focusing on the fundamental trends and boundaries within which these blue-cloud galaxies are able to continue growing through star formation. This kind of approach should not be affected by progenitor effects or size growth through dry/minor mergers. Thus the observations that the leading edge of the blue cloud in the size-mass plane in Figs. 9–13 is tilted to run parallel to lines of constant M/r_e or σ_{inf} , rather than vertical, implies that the fundamental limit beyond which galaxies cannot continue to form stars depends significantly on galaxy size. Larger galaxies can continue to form stars to higher stellar masses than smaller galaxies. Figure 10 shows how this limit retreats systematically to lower stellar masses by 0.17 dex from the $0.7 < z < 1.0$ bin to that at $0.5 < z < 0.7$. This appears as concrete evidence of downsizing of star-formation at these redshifts. Similarly, Moustakas et al. (2013) find that the stellar mass M_c at fixed cumulative number density $n(M > M_c) = 10^{-3.5} \text{ Mpc}^{-3}$ of the most massive star-forming galaxies decreases by 0.18 ± 0.05 dex since $z = 1$, while Brammer et al. (2011) find a ~ 0.2 dex decrease in M_c between $z = 2$ and $z = 0.5$.

As blue-cloud galaxies approach the high-mass limit, their d4000 values start to increase, pushing them to the high-d4000 wing of the blue cloud ($1.40 < \text{d4000} < 1.55$). These are the galaxies most likely to be quenched in the near future and subsequently join the red sequence. These quenching galaxies lie within a diagonal band (0.6–0.7 dex wide), between the two black dashed lines in Fig. 9a ($100 < \sigma_{\text{inf}} < 225 \text{ km s}^{-1}$), which can be considered the quenching zone for galaxies at these redshifts. The fact that this quenching zone runs diagonally, combined with the 1 dex range in effective radii of blue-cloud galaxies, means that the range of stellar masses where galaxies are being quenched ($0.1\text{--}3 \times 10^{11} M_\odot$) is much wider than the width of the quenching zone at fixed size. Whitaker et al. (2017) obtain very similar trends when examining the average specific-SFRs of UVJ-selected star-forming galaxies as a function of their location within the size-mass plane, with the specific-SFRs falling for galaxies along the leading edge of the blue cloud at $0.5 < z < 1.0$. There are some hints of these trends even within their $1.5 < z < 2.5$ redshift bin.

Figures 12 and 13 show that the structures of blue-cloud galaxies in the quenching zone have already changed, having Sérsic indices $\eta \gtrsim 2$ and high central stellar mass densities $\Sigma_1 > 10^{9.0} M_\odot \text{ kpc}^{-2}$. Bulge growth is necessary for these galaxies to reach the high-mass limit of the blue cloud and be quenched. Lang et al. (2014) show a marked increase in the Sérsic index and B/T ratios of star-forming galaxies with stellar masses above $10^{11} M_\odot$ at $0.5 < z < 2.5$ (in both redshift bins examined). They also find that the fraction of quenched galaxies correlates strongly with bulge mass, but not with disc mass. At fixed disc mass, the fraction of quenched galaxies increases rapidly with B/T ratio.

Notably, the *quenching zone* of $z \sim 0.8$ blue-cloud galaxies lies precisely along the same size-mass relation as quiescent galaxies in the local Universe (Fig. 8c). Given that these galaxies have already changed their structures and have dense centres, these quenching galaxies do not seem to have to evolve much further beyond terminating their star formation. These objects would seem to be likely progenitors for today's S0 population.

Given the well-known tight correlation between the mass of the central supermassive black hole (M_\bullet) and the velocity

dispersion of its host galaxy (e.g., Kormendy & Ho 2013), the alignment of the quenching zone and the edge of the blue cloud with lines of constant σ_{inf} is suggestive of AGN feedback playing a role in the quenching process. van den Bosch (2016) obtain a best-fit relation between black hole mass M_\bullet , stellar mass, and size of the form $\log_{10}(M_\bullet/M_\odot) = 7.48 + 2.91 \log_{10}(M/10^{11} M_\odot) - 2.77 \times \log_{10}(r_e/5 \text{ kpc})$, or $M_\bullet \propto (M/r_e)^{2.9}$. As galaxies traverse the quenching zone, their central black hole mass should thus increase by two orders of magnitude, from $M_\bullet = 10^{6.28} M_\odot$ on the 100 km s^{-1} line to $M_\bullet = 10^{8.33} M_\odot$ as they reach the 225 km s^{-1} line in our size-mass figures. Heckman & Best (2014) show that radiative-mode AGN with accretion rates $> 1\%$ of the Eddington limit are preferentially hosted in blue-cloud ($\text{d4000} < 1.6$) galaxies with high stellar mass densities, exactly describing the galaxies in our quenching zone.

Figures 13b and c show that high central stellar mass densities ($\Sigma_1 > 10^{9.0} M_\odot \text{ kpc}^{-2}$) appear necessary for a galaxy to have become quiescent ($\text{d4000} > 1.55$), as seen previously (Bell 2008; Bell et al. 2012). This threshold in Σ_1 also happens to run parallel to the high-mass edge of the blue-cloud population, and lines of constant d4000 values. This supports the idea that quenching of star formation is linked to the presence of a dense central stellar mass concentration in a galaxy. It is not that surprising that the most massive star-forming galaxies have different structures to their lower mass counterparts. Using the evolving SFR– M relations of Tomczak et al. (2016) as before to predict the star formation histories of blue-cloud galaxies as a function of stellar mass, the most massive blue-cloud galaxies in VIPERS ($M > 10^{11} M_\odot$) should have had their SFR peak at $z \sim 2$ (Fig. C.1), before it declines by a factor 3–5 by $z \sim 0.8$. Thus, the bulk of their stellar mass would have been assembled when the galaxy was much smaller and denser, and naturally forms a bulge-like central mass concentration (without considering any possible compaction process). Blue-cloud galaxies that have $M \sim 10^{10.5} M_\odot$ at $z \sim 0.8$ only had their peak SFR at $z \sim 1.0\text{--}1.2$, and so the bulk of star formation occurred when the galaxy is close to its present size, meaning no significant change in structure.

At higher redshifts, Tacchella et al. (2015) show that massive star-forming galaxies at $z \sim 2.2$ (with $\text{SFRs} \sim 20\text{--}300 M_\odot$, placing them on the main star-forming sequence at that redshift) already host fully grown bulges with the high central stellar mass densities of present day quiescent ellipticals, and show evidence of inside-out quenching. They suggest that the high central stellar mass densities of these massive star-forming galaxies arise through gas-rich dissipative processes such as violent disc instabilities leading to a compaction of the gas disc (Dekel & Burkert 2014; Zolotov et al. 2015; Tacchella et al. 2016). This central mass concentration (bulge) could then induce morphological or gravitational quenching by stabilizing the remaining gas disc against fragmentation into molecular clouds (Martig et al. 2009), quenching star formation from the inside out, resulting in central dips in the star-formation efficiency or rings of star formation in the outer disc (Genzel et al. 2014).

The relative narrowness of the quenching zone and the associated global changes in structure are indicative of a rather rigid, uniform transformation that affects most, if not all, star-forming galaxies once they enter the zone, and indeed before, given the rather tight SFR– M relation of star-forming galaxies with intrinsic scatter of 0.2–0.3 dex (Noeske et al. 2007; Speagle et al. 2014; Lee et al. 2015). This uniformity would appear at odds with the merger-driven quasar feedback model of Hopkins et al. (2006), whereby massive star-forming galaxies are quenched as

the result of infrequent, extreme events. This uniformity could instead suggest that galaxies follow rather well-defined evolutionary tracks, and that quenching is less a specific event, but a normal continuation of their late-stage evolution (Gladders et al. 2013; Abramson et al. 2016).

7. Summary

We have used the full VIPERS redshift survey in combination with SDSS-DR7 to explore the relationships between star-formation history (as quantified using d4000), stellar mass and galaxy structure, and establish the limiting galaxy properties beyond which they are unable to continue growing via star formation, and how these limits evolve from $z \sim 1$ to the present day.

- We measured the d4000 distributions of galaxies in narrow bins of stellar mass to establish the locations and dispersions of both the blue cloud and red sequence populations as a function of stellar mass and redshift. We identify the upper limit of the blue cloud as the first stellar mass bin where no appreciable peak or feature is visible in the d4000 distribution at values indicative of young stellar populations ($d4000 < 1.55$). The high-mass limit is seen to retreat steadily with time from $M \sim 10^{11.2} M_{\odot}$ at $z \sim 0.9$ to $M \sim 10^{10.7} M_{\odot}$ in galaxies from the SDSS-DR7.
- The comoving number density of massive blue-cloud galaxies ($M > 10^{11} M_{\odot}$, $d4000 < 1.55$) is also seen to decline by a factor 4–5 between $z \sim 0.8$ to $z \sim 0.5$ within the VIPERS dataset. These massive galaxies are being quenched in large numbers at $z \sim 0.7$ and contribute to the rapid increase in the number densities of massive passive galaxies seen to occur over this period.
- The star formation histories of galaxies are seen to depend on their size (r_e), as well as stellar mass, with larger galaxies having younger stellar populations than smaller ones at fixed stellar mass. Galaxies with the same d4000 values align themselves along lines of constant M/r_e or σ_{inf} in the size-mass plane.
- The upper limit of the blue cloud population also runs along a line of constant M/r_e . As star-forming galaxies grow and approach this limit, their d4000 values start to increase, pushing them towards the green valley. Their structures are also showing systematic changes, with Sérsic indices $\eta \gtrsim 2.5$ more characteristic of early-type galaxies, and high central stellar mass densities $\Sigma_1 \gtrsim 10^{9.0} M_{\odot} \text{ kpc}^{-2}$. These trends are seen both for VIPERS galaxies at $0.5 \leq z < 1.0$ and SDSS galaxies in the local Universe.
- The massive star-forming galaxies that leave the blue cloud at $z \sim 0.8$, already lie along size-mass relation of present day quiescent galaxies, and seemingly have to do relatively little beyond stopping forming stars to become today's S0s.

Acknowledgements. We acknowledge the crucial contribution of the ESO staff for the management of service observations. In particular, we are deeply grateful to M. Hilker for his constant help and support of this program. Italian participation to VIPERS has been funded by INAF through PRIN 2008, 2010, and 2014 programs. L.G. and B.R.G. acknowledge support from the European Research Council through grant No. 291521. O.L.F. acknowledges support from the European Research Council through grant No. 268107. J.A.P. acknowledges support of the European Research Council through grant No. 67093. R.T. acknowledges financial support from the European Research Council through grant No. 202686. A.P., K.M., J.K. and M.S. have been supported by the National Science Centre (grants UMO-2012/07/B/ST9/04425 and UMO-2013/09/D/ST9/04030). E.B., F.M. and L.M. acknowledge the support from grants ASI-INAf I/023/12/0 and PRIN MIUR 2010-2011. L.M. also acknowledges financial support from PRIN INAF 2012. T.M. and S.A. acknowledge

financial support from the ANR Spin(e) through the french grant ANR-13-BS05-0005. S.D.L.T. and M.P. acknowledge the support of the OCEVU Labex (ANR-11-LABX-0060) and the A*MIDEX project (ANR-11-IDEX-0001-02) funded by the “Investissements d’Avenir” French government program managed by the ANR and the Programme National Galaxies et Cosmologie (PNCG). Research conducted within the scope of the HECOLS International Associated Laboratory, supported in part by the Polish NCN grant DEC-2013/08/M/ST9/00664.

References

- Abazajian, K. N., Adelman-McCarthy, J. K., & Agueros, M. 2009, *ApJS*, **182**, 543
- Abramson, L. E., Gladders, M. D., Dressler, A., et al. 2016, *ApJ*, **832**, 7
- Arnouts, S., Walcher, C. J., Le Fèvre, O., et al. 2007, *A&A*, **476**, 137
- Arnouts, S., Le Floc’h, E., Chevillard, J., et al. 2013, *A&A*, **558**, A67
- Baldry, I. K., Glazebrook, K., Brinkmann, J., et al. 2004, *ApJ*, **600**, 681
- Ball, N. M., Loveday, J., & Brunner, R. J. 2007, *MNRAS*, **383**, 907
- Balogh, M. L., Morris, S. L., Yee, H. K. C., Carlberg, R. G., & Ellingson, E. 1999, *ApJ*, **527**, 54
- Barro, G., Faber, S. M., Koo, D. C., et al. 2017, *ApJ*, **840**, 47
- Behroozi, P. S., Wechsler, R. J., & Conroy, C. 2013, *ApJ*, **770**, 57
- Bell, E. F. 2008, *ApJ*, **682**, 355
- Bell, E. F., Zheng, X. Z., Papovich, C., et al. 2007, *ApJ*, **663**, 834
- Bell, E. F., van der Wel, A., Papovich, C., et al. 2012, *ApJ*, **753**, 167
- Bezanson, R., van Dokkum, P., Franx, M., et al. 2011, *ApJ*, **737**, L31
- Blanton, M. R., & Moustakas, J. 2009, *ARA&A*, **47**, 159
- Bolzonella, M., Miralles, J. M., & Pelló, R. 2000, *A&A*, **363**, 476
- Bolzonella, M., Kovac, K., & Pozzetti, L. 2010, *A&A*, **524**, A76
- Borch, A., Meisenheimer, K., & Bell, E. F. 2006, *A&A*, **453**, 869
- Bouchet, P., Lequeux, J., Maurice, E., Prevot, L., & Prevot-Burnichon, M. L. 1985, *A&A*, **149**, 330
- Bower, R. G., Benson, A. J., Malbon, R., et al. 2006, *MNRAS*, **370**, 645
- Brammer, G. B., Whitaker, K. E., van Dokkum, P. G., et al. 2011, *ApJ*, **739**, 24
- Brinchmann, J., Charlot, S., White, S. D. M., et al. 2004, *MNRAS*, **351**, 1151
- Bruce, V. A., Dunlop, J. S., McLure, R. J., et al. 2014, *MNRAS*, **444**, 1001
- Bruzual, G., & Charlot, S. 2003, *MNRAS*, **344**, 1000
- Buitrago, F., Trujillo, I., Conselice, C. J., et al. 2008, *ApJ*, **687**, L61
- Bundy, K., Ellis, R. S., Conselice, C. J., et al. 2006, *ApJ*, **651**, 120
- Calzetti, D., Armus, L., Bohlin, R. C., et al. 2000, *ApJ*, **533**, 682
- Cappellari, M., McDermid, R. M., Alatalo, K., et al. 2013, *MNRAS*, **432**, 1862
- Chabrier, G. 2003, *PASP*, **115**, 763
- Chen, Y.-M., Kauffmann, G., Tremonti, C. A., et al. 2012, *MNRAS*, **421**, 314
- Cheung, E., Faber, S. M., Koo, D. C., et al. 2012, *ApJ*, **760**, 131
- Conroy, C., van Dokkum, P. G., & Kravtsov, A. 2015, *ApJ*, **803**, 77
- Cowie, L. L., Songaila, A., Hu, E. M., & Cohen, J. G. 1996, *AJ*, **112**, 839
- Croton, D., Springel, V., White, S. D. M., et al. 2006, *MNRAS*, **365**, 11
- Davidzon, I., Bolzonella, M., Coupon, J., et al. 2013, *A&A*, **558**, A23
- Davidzon, I., Cucciati, O., Bolzonella, A., et al. 2016, *A&A*, **586**, A23
- Dekel, A., & Birnboim, Y. 2006, *MNRAS*, **368**, 2
- Dekel, A., & Burkert, A. 2014, *MNRAS*, **438**, 1870
- Dekel, A., Birnboim, Y., Engel, G., et al. 2009, *Nature*, **457**, 451
- Di Matteo, T., Springel, V., & Hernquist, L. 2005, *Nature*, **433**, 604
- Driver, S. P., & Robotham, A. S. G. 2010, *MNRAS*, **407**, 2131
- Driver, S. P., Allen, P. D., Graham, A. W., et al. 2006, *MNRAS*, **368**, 414
- Elbaz, D., Daddi, E., Le Borgne, D., et al. 2007, *A&A*, **468**, 33
- Fall, S. M., & Efstathiou, G. 1980, *MNRAS*, **193**, 189
- Fang, J. J., Faber, S. M., Koo, D. C., & Dekel, A. 2013, *ApJ*, **776**, 63
- Fontanot, F., De Lucia, G., Monaco, P., Somerville, R. S., & Santini, P. 2009, *MNRAS*, **397**, 1776
- Franx, M., van Dokkum, P., Förster Schreiber, N. M., et al. 2008, *ApJ*, **688**, 770
- Fritz, A., Scoddeggio, M., Ilbert, O., et al. 2014, *A&A*, **563**, A92
- Gabor, J. M., Davé, R., Finlator, K., & Oppenheimer, B. D., 2010, *MNRAS*, **407**, 749
- Gallazzi, A., Charlot, S., Brinchmann, J., White, S. D. M., & Tremonti, C. A. 2005, *MNRAS*, **362**, 41
- Garilli, B., Fumana, M., & Franzetti, P., et al. 2010, *PASP*, **122**, 827
- Garilli, B., Paoiro, L., & Scoddeggio, M., et al. 2012, *PASP*, **124**, 1232
- Garilli, B., Guzzo, L., Scoddeggio, M., et al. 2014, *A&A*, **562**, A23
- Gargiulo, A., Bolzonella, M., Scoddeggio, M., et al. 2016, *A&A* in press, DOI: 10.1051/0004-6361/201630112
- Genzel, R., Förster Schreiber, N. M., Lang, P., et al. 2014, *ApJ*, **785**, 75
- Gladders, M. D., Oemler, A., Dressler, A., et al. 2013, *ApJ*, **770**, 64
- González Delgado, R. M., García-Benito, R., Pérez, E., et al. 2015, *A&A*, **581**, A103
- Gorgas, J., Cardiel, N., Pedraz, S., & González, J. J. 1999, *A&AS*, **139**, 29
- Guzzo, L., Scoddeggio, M., Garilli, B., et al. 2014, *A&A*, **566**, A108

- Haines, C. P., La Barbera, F., Mercurio, A., Merluzzi, P., & Busarello, G. 2006, *ApJ*, **647**, L21
- Haines, C. P., Gargiulo, A., & La Barbera, F. 2007, *MNRAS*, **381**, 7
- Haines, C. P., Gargiulo, A., & Merluzzi, P. 2008, *MNRAS*, **385**, 1201
- Heckman, T. M., & Best, P. N. 2014, *ARA&A*, **52**, 589
- Hopkins, P. F., Hernquist, L., Cox, T. J., et al. 2006, *ApJ*, **163**, 1
- Hubble, E. P. 1926, *ApJ*, **64**, 321
- Ilbert, O., Salvato, M., Le Floc'h, E., et al. 2010, *ApJ*, **709**, 644
- Ilbert, O., McCracken, H. J., Le Fèvre, O., et al. 2013, *A&A*, **556**, A55
- Iovino, A., Petropoulou, V., Scoddeggio, M., et al. 2016, *A&A*, **592**, A78
- Jarvis, M. J., Bonfield, D. G., Bruce, V. A., et al. 2013, *MNRAS*, **428**, 1281
- Kauffmann, G., Heckman, T. M., White, S. D. M., et al. 2003a, *MNRAS*, **341**, 54
- Kauffmann, G., Heckman, T. M., White, S. D. M., et al. 2003b, *MNRAS*, **341**, 33
- Kauffmann, G., Heckman, T. M., de Lucia, G., et al. 2006, *MNRAS*, **367**, 1394
- Kereš, D., Katz, N., Weinberg, D. H., & Davé, R. 2005, *MNRAS*, **363**, 2
- Kewley, L. J., Jansen, R. A., & Geller, M. J. 2005, *PASP*, **117**, 227
- Knobel, C., Lilly, S. J., Iovino, A., et al. 2012, *ApJ*, **753**, 121
- Kormendy, J., & Bender, R. 2012, *ApJS*, **198**, 2
- Kormendy, J., & Ho, L. C. 2013, *ARA&A*, **51**, 511
- Krywult, J., Tasca, L. A. M., Pollo, A., et al. 2017, *A&A*, **598**, A120
- Lang, P., Wuyts, S., Somerville, R. S., et al. 2014, *ApJ*, **788**, 11
- Lee, N., Sanders, D. B., Casey, C. M., et al. 2015, *ApJ*, **801**, 80
- Le Fèvre, O., Saisse, M., Mancini, D., et al. 2003, *SPiE*, **4841**, 1670
- Le Fèvre, O., Vettolani, G., Garilli, B., et al. 2005, *A&A*, **439**, 845
- Lilly, S. J., & Carollo, C. M. 2016, *ApJ*, **833**, 1
- Lilly, S. J., Le Fèvre, O., Renzini, A., et al. 2007, *ApJS*, **172**, 70
- Lilly, S. J., Le Brun, V., Maier, C., et al. 2009, *ApJS*, **184**, 218
- Macciò, A. V., Dutton, A. A., & van den Bosch, F. C. 2008, *MNRAS*, **391**, 1940
- Mahajan, S., Haines, C. P., & Raychaudhury, S. 2010, *MNRAS*, **404**, 1745
- Martig, M., Bornaud, F., Teyssier, R., & Dekel, A. 2009, *ApJ*, **707**, 250
- McDermid, R. M., Alatalo, K., Blitz, L., et al. 2015, *MNRAS*, **448**, 3484
- Mo, H. J., Mao, S., & White, S. D. M. 1998, *MNRAS*, **295**, 319
- Mosleh, M., Williams, R. J., Franx, M., et al. 2012, *ApJ*, **756**, 12
- Moster, B. P., Naab, T., & White, S. D. M. 2013, *MNRAS*, **428**, 3121
- Moustakas, J., Coil, A. L., Aird, J., et al. 2013, *ApJ*, **767**, 50
- Moutard, T., Arnouts, S., Ilbert, O., et al. 2016a, *A&A*, **590**, A102
- Moutard, T., Arnouts, S., Ilbert, O., et al. 2016b, *A&A*, **590**, A103
- Muzzin, A., Marchesini, D., Stefanon, M., et al. 2013, *ApJ*, **777**, 18
- Nelson, E. J., van Dokkum, P. G., Förster Schreiber, N., et al. 2016, *ApJ*, **828**, 27
- Newman, A. B., Ellis, R. S., Bundy, K., & Treu, T. 2012, *ApJ*, **746**, 162
- Noeske, K. G., Weiner, B. J., Faber, S. M., et al. 2007, *ApJ*, **660**, 43
- Omand, C. M. B., Balogh, M. L., & Poggianti, B. M. 2014, *MNRAS*, **440**, 843
- Patel, S. G., van Dokkum, P. G., Franx, M., et al. 2013, *ApJ*, **766**, 15
- Peng, Y.-J., Lilly, S. J., Kovac, K., et al. 2010, *ApJ*, **721**, 193
- Pisani, A. 1993, *MNRAS*, **265**, 706
- Pozzetti, L., Bolzonella, M., Zucca, E., et al. 2010, *A&A*, **523**, A13
- Prevot, M. L., Lequeux, J., Prevot, L., Maurice, E., & Rocca-Volmerange, B., 1984, *A&A*, **132**, 389
- Salim, S., Rich, M. R., Charlot, S., et al. 2007, *ApJS*, **173**, 267
- Sandage, A. 1961, *The Hubble Atlas of Galaxies* (Washington DC: Carnegie Institution of Washington)
- Schmidt, M. 1968, *ApJ*, **151**, 393
- Scoddeggio, M., Franzetti, P., Garilli, B., Le Fèvre, O., & Guzzo, L. 2009, *The Messenger*, **135**, 13
- Scoddeggio, M., Guzzo, L., Garilli, B., et al. 2017, *A&A*, in press, DOI: 10.1051/0004-6361/201630114
- Shetty, S., & Cappellari, M. 2015, *MNRAS*, **454**, 1332
- Silverman, B. W. 1986, *Density Estimation for Statistics and Data Analysis* (London: Chapman & Hall)
- Simard, L., Mendel, J. T., Patton, D. R., Ellison, S. L., & McConnell, A. W. 2011, *ApJS*, **196**, 11
- Siudek, M., Malek, K., Scoddeggio, M., et al. 2017, *A&A*, **597**, A107
- Speagle, J. S., Steinhardt, C. L., Capak, P. L., & Silverman, J. D. 2014, *ApJS*, **214**, 15
- Strateva, I., Ivezić Ž., Knapp, G. R., et al. 2001, *AJ*, **122**, 1861
- Tacchella, S., Carollo, C. M., Renzini, A., et al. 2015, *Science*, **348**, 314
- Tacchella, S., Dekel, A., Carollo, C. M., et al. 2016, *MNRAS*, **457**, 2790
- Taylor, E. N., Franx, M., Glazebrook, K., et al. 2010, *ApJ*, **720**, 723
- Taylor, E. N., Hopkins, A. M., Baldry, I. K., et al. 2015, *MNRAS*, **446**, 2144
- Thomas, D., Maraston, C., Bender, R., & Mendes de Oliveira, C. 2005, *ApJ*, **621**, 673
- Tomczak, A. R., Quadri, R. F., Tran, K.-V. H., et al. 2014, *ApJ*, **783**, 85
- Tomczak, A. R., Quadri, R. F., Tran, K.-V. H., et al. 2016, *ApJ*, **817**, 118
- van den Bosch, R. C. E. 2016, *ApJ*, **831**, 134
- van der Wel, A., Franx, M., van Dokkum, P. G., et al. 2014, *ApJ*, **788**, 28
- van Dokkum, P. G., Whitaker, K. E., Brammer, G., et al. 2010, *ApJ*, **709**, 1018
- Vergani, D., Scoddeggio, M., Pozzetti, L., et al. 2008, *A&A*, **487**, 89
- Whitaker, K., Franx, M., Leja, J., et al. 2014, *ApJ*, **795**, 104
- Whitaker, K., Bezanson, R., van Dokkum, P. G., et al. 2017, *ApJ*, **838**, 19
- Wuyts, S., Förster Schreiber, N. M., van der Wel, A., et al. 2011, *ApJ*, **742**, 96
- Wyder, T. K., Martin, D. C., Schiminovich, D., et al. 2007, *ApJS*, **173**, 293
- Yang, X., Mo, H. J., van den Bosch, F. C., Zhang, Y., & Han, J. 2012, *ApJ*, **752**, 41
- Zolotov, A., Dekel, A., Mandelker, N., et al. 2015, *MNRAS*, **450**, 2327
- Zjupa, J., & Springel, V. 2017, *MNRAS*, **466**, 1625

- 1 INAF–Osservatorio Astronomico di Brera, via Brera 28, 20121 Milano, via. E. Bianchi 46, 23807 Merate, Italy
e-mail: chris.haines@oa-brera.inaf.it
- 2 Institute of Physics, Jan Kochanowski University, ul. Świetokrzyska 15, 25-406 Kielce, Poland
- 3 Università degli Studi di Milano, via G. Celoria 16, 20133 Milano, Italy
- 4 Aix-Marseille Univ., CNRS, LAM, Laboratoire d’Astrophysique de Marseille, 13388 Marseille, France
- 5 INAF–Osservatorio Astronomico di Bologna, via Gobetti 93/3, 40129 Bologna, Italy
- 6 INAF–Istituto di Astrofisica Spaziale e Fisica Cosmica Milano, via Bassini 15, 20133 Milano, Italy
- 7 INAF–Osservatorio Astronomico di Trieste, via G. B. Tiepolo 11, 34143 Trieste, Italy
- 8 INAF–Osservatorio Astronomico di Torino, 10025 Pino Torinese, Italy
- 9 Dipartimento di Fisica e Astronomia – Alma Mater Studiorum Università di Bologna, viale Berti Pichat 6/2, 40127 Bologna, Italy
- 10 Laboratoire Lagrange, UMR 7293, Université de Nice Sophia Antipolis, CNRS, Observatoire de la Côte d’Azur, 06300 Nice, France
- 11 National Centre for Nuclear Research, ul. Hoza 69, 00-681 Warszawa, Poland
- 12 INFN, Sezione di Bologna, viale Berti Pichat 6/2, 40127 Bologna, Italy
- 13 Aix-Marseille Université, Jardin du Pharo, 58 bd Charles Livon, 13284 Marseille Cedex 7, France
- 14 IRAP, 9 Av. du colonel Roche, BP 44346, 31028 Toulouse Cedex 4, France
- 15 Astronomical Observatory of the Jagiellonian University, Orla 171, 30-001 Cracow, Poland
- 16 School of Physics and Astronomy, University of St Andrews, St Andrews KY16 9SS, UK
- 17 INAF – Istituto di Astrofisica Spaziale e Fisica Cosmica Bologna, via Gobetti 101, 40129 Bologna, Italy
- 18 INAF – Istituto di Radioastronomia, via Gobetti 101, 40129, Bologna, Italy
- 19 Canada-France-Hawaii Telescope, 65–1238 Mamalahoa Highway, Kamuela, HI 96743, USA
- 20 Aix-Marseille Univ., Univ. Toulon, CNRS, CPT, 13013 Marseille, France
- 21 Dipartimento di Matematica e Fisica, Università degli Studi Roma Tre, via della Vasca Navale 84, 00146 Roma, Italy
- 22 INFN, Sezione di Roma Tre, via della Vasca Navale 84, 00146 Roma, Italy
- 23 INAF–Osservatorio Astronomico di Roma, via Frascati 33, 00040 Monte Porzio Catone (RM), Italy
- 24 Astronomical Observatory of the University of Geneva, Ch. d’Ecogia 16, 1290 Versoix, Switzerland
- 25 Department of Astronomy & Physics, Saint Mary’s University, 923 Robie Street, Halifax, Nova Scotia, B3H 3C3, Canada
- 26 Institute for Astronomy, University of Edinburgh, Royal Observatory, Blackford Hill, Edinburgh EH9 3HJ, UK
- 27 Center for Theoretical Physics, Al. Lotnikow 32/46, 02-668 Warsaw, Poland

Appendix A: Stellar mass completeness limits

For magnitude-limited surveys such as VIPERS, the minimum stellar mass M_{lim} to which a galaxy would be targeted depends on both its redshift and its stellar mass-to-light ratio M/L . The mass-to-light ratio depends on the star-formation history of the galaxy, and so should be a simple function of $d4000$. We apply the technique of Pozzetti et al. (2010) to derive the stellar mass completeness limits of the VIPERS survey for each redshift bin. The limiting stellar mass (M_{lim}) of each galaxy within the VIPERS spectroscopic sample is obtained as the mass it would have if its i -band apparent magnitude were equal to the limiting magnitude of the survey ($i_{\text{lim}} = 22.5$), given by $\log_{10}(M_{\text{lim}}) = \log_{10}(M) + 0.4(i - i_{\text{lim}})$. Figure A.1 plots the resulting distribution of M_{lim} for galaxies (light blue points) within the $0.50 \leq z < 0.65$ redshift interval as a function of their $d4000$ value.

We measure the median M_{lim} value of these galaxies as a function of $d4000$ (blue curve), as well as the 90th percentile (upper dashed curve). The M_{lim} appears to be relatively independent of $d4000$ for large values (≥ 1.6) indicative of quiescent galaxies, but falls exponentially with decreasing $d4000$ for $d4000 \lesssim 1.4$. We model this by fitting the 90th percentile curve with a double power law (red curve), that is fixed to become asymptotically constant at large $d4000$ values. This process is repeated for our other redshift intervals (black curves). These power laws represent the 90% completeness limits of VIPERS as a function of $d4000$ shown by the dashed curves in Fig. 3. This can be understood as 90% of galaxies in our spectroscopic sample within that redshift interval have stellar mass limits below the curve, and so would be brighter than the $i = 22.5$ survey limit if they were rescaled to have a stellar mass placing them on the curve given their $d4000$ value.

Appendix B: Size-mass relation coded by the bulge-to-total ratio

Simard et al. (2011) performed full bulge-disc decompositions, with $\eta = 4$ bulge and exponential disc components, for all SDSS-DR7 galaxies in our sample. Figure B.1 replots the size-mass relation of blue-cloud galaxies ($d4000 < 1.55$) at $0.02 \leq z < 0.08$ from the SDSS-DR7, colour coded according to the fraction of r -band galaxian light due to the bulge component (B/T). For galaxies which have two distinct components, a single Sérsic function may have difficulty fitting the radial light profile at all radii, and so in these cases the B/T ratio should be more robust measure of galaxy structure.

Galaxies on the leading edge of the blue cloud have significant bulge components ($0.3 \lesssim (B/T) \lesssim 1.0$), as do the most compact systems ($r_e \lesssim 1.5$ kpc) at all stellar masses, while the remaining low-mass galaxies are uniformly disc-dominated ($B/T < 0.25$). This confirms that the changes in galaxy structure reported in Fig. 12 based on their Sérsic indices, for blue-cloud galaxies along the high-mass edge of the blue cloud, do reflect concrete changes in galaxy structure.

Appendix C: Growth and evolution of star-forming galaxies as a function of stellar mass

We use the parametrized functions describing the redshift evolution of the SFR- M relation of UVJ-selected star-forming galaxies from Tomczak et al. (2016) to predict the stellar mass growth of star-forming galaxies as a function of redshift. The

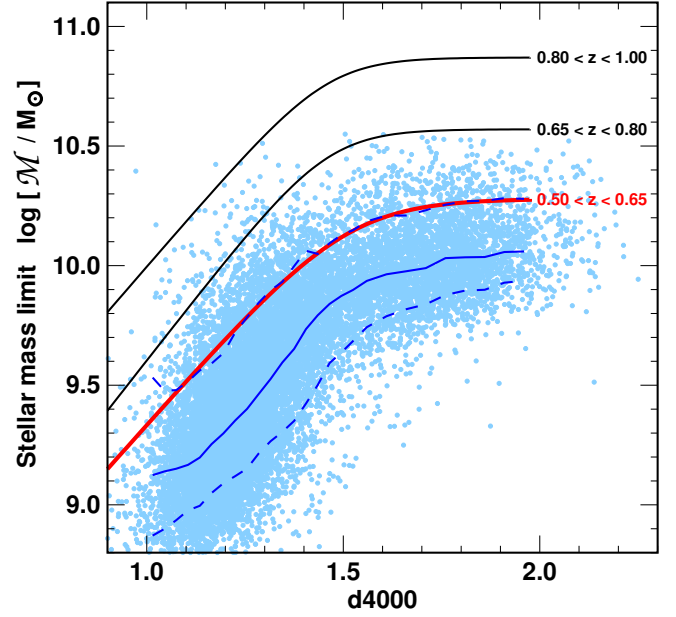


Fig. A.1. Stellar mass completeness limits as a function of $d4000$ and redshift. Light blue points mark the limiting stellar mass (M_{lim}) of $0.50 \leq z < 0.65$ VIPERS galaxies, at which they would have the apparent magnitude limit $i_{\text{AB}} = 22.5$ of the survey. The solid blue curve marks the median M_{lim} value of these galaxies as a function of $d4000$, while the dashed lines mark the 16% and 90% completeness limits. The red curve is the best-fit double power-law to the 90% completeness limit for galaxies within the $0.50 \leq z < 0.65$ redshift bin. Black curves plot the corresponding best-fit double power-laws to the 90% completeness limits for the $0.65 \leq z < 0.80$ and $0.80 \leq z < 1.00$ redshift intervals.

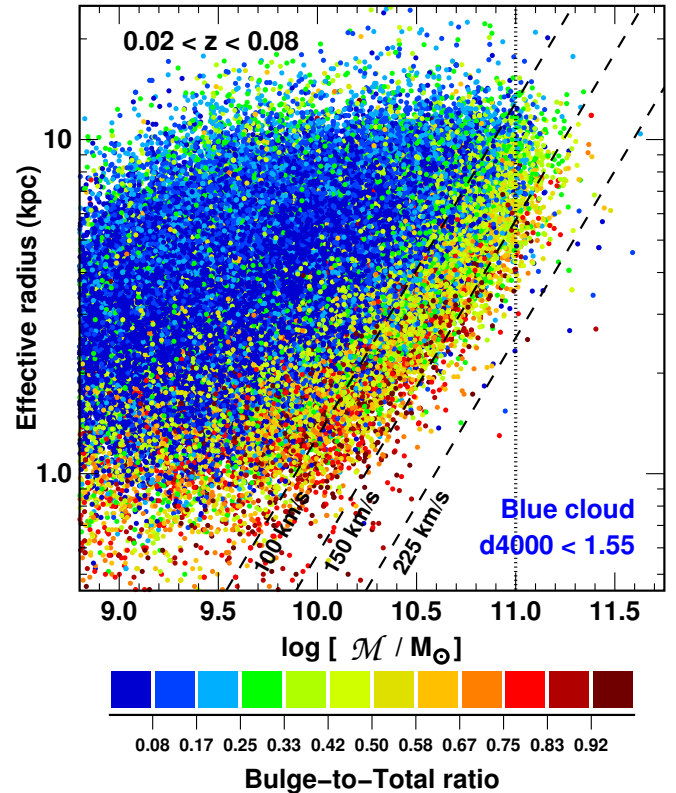


Fig. B.1. Size-mass relation of SDSS blue-cloud galaxies ($d4000 < 1.55$) in the local Universe ($0.02 \leq z < 0.08$). Galaxies are colour coded according to their bulge-to-total (B/T) ratio derived by Simard et al. (2011).

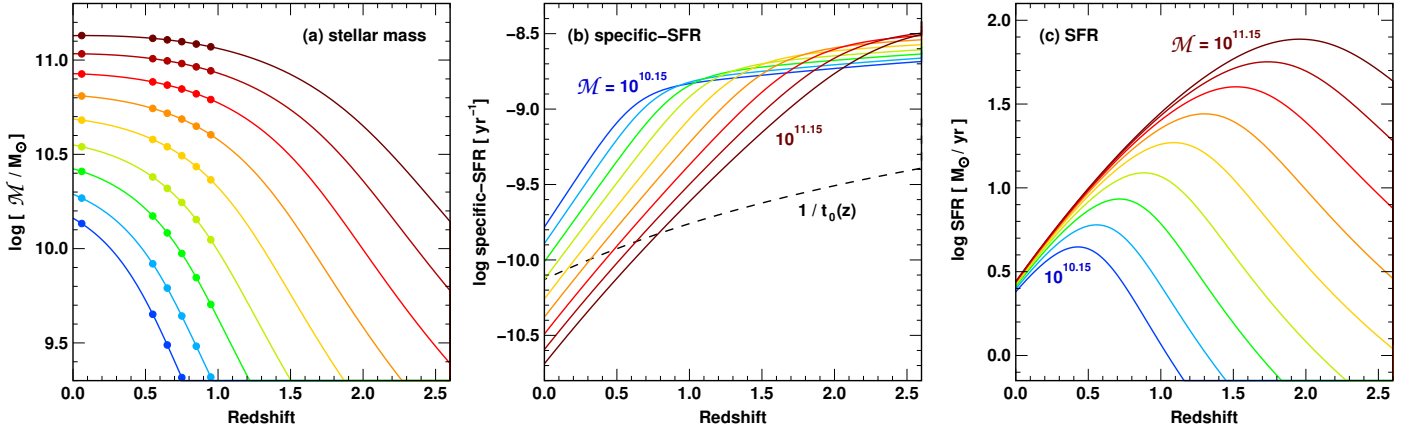


Fig. C.1. Mass growth profiles (*left*), specific-SFRs (*centre*) and SFRs (*right*) extracted from the evolution of the SFR– M relation of star-forming galaxies of Tomczak et al. (2016). Mass loss owing to stellar evolution is accounted for according to Eq. (16) of Moster et al. (2013). The coloured curves indicate how the evolution of galaxies that evolve along the main star-forming sequence varies as a function of their final stellar mass, from low-mass galaxies ($M = 10^{10.15} M_{\odot}$; blue) to those near the high-mass limit of the blue cloud ($10^{11.15} M_{\odot}$; dark red).

relations are based on observations of $0.5 < z < 4$ star-forming galaxies from the FourStar Galaxy Evolution Survey (ZFOURGE) in combination with far-infrared imaging from *Spitzer* and *Herschel*. We start with a seed galaxy at redshift 4.0, and initial stellar mass M_0 , from which we calculate its predicted SFR at that redshift from the parameterized SFR– M relation given in Eq. (4) of Tomczak et al. (2016). In time steps equal to $\Delta z = 0.01$, the stellar mass is shifted by the amount of star formation added according to its SFR. SFRs are recalculated at each new time step. Mass loss owing to stellar evolution is accounted for according to Eq. (16) of Moster et al. (2013). We then evolve the observed stellar mass $M(z)$ of the galaxy forward in time to the present day. We repeat this for a number of seed galaxies with a range of initial stellar masses, in order to populate the observed stellar mass range of star-forming galaxies at $z = 0$. The resulting mass growth profiles $M(z)$ are shown in Fig. C.1a by the coloured curves, from low-mass (blue) to high-mass (red) galaxies.

The evolutions of the specific-SFRs, $\text{SFR}(z)/M(z)$, of the same galaxies and their SFRs are shown in Figs. C.1b and c. The black dashed curve in Fig. C.1b indicates the evolution of $1/t_0(z)$ where $t_0(z)$ is the age of the Universe at redshift z in yr. The specific-SFRs of star-forming galaxies of all masses remain relatively constant at high redshifts at values of $\sim 10^{-8.6} \text{ yr}^{-1}$ and little dependency on mass. Starting with the most massive star-forming galaxies they progressively peel off this phase of flat specific-SFRs, and start a second phase of steady decline in specific-SFR that continues unabated to the present day. Massive star-forming galaxies can be seen to follow an accelerated evolution relative to their lower mass counterparts. Similarly, the SFRs of star-forming galaxies peak at a redshift that increases with stellar mass (Fig. C.1c), from $z_{\text{peak}} \sim 0.5$ for low-mass systems which have $M \sim 10^{10.15} M_{\odot}$ at $z = 0$, to $z_{\text{peak}} \sim 2.0$ for those which become today's most massive blue-cloud galaxies with $M \sim 10^{11.15} M_{\odot}$.